



Mechanochemically tailoring oxygen vacancies of MnO₂ for efficient degradation of tetrabromobisphenol A with peroxyomonosulfate

Sylvestre Ndayiragije ^a, Yifan Zhang ^a, Yuqi Zhou ^b, Zhou Song ^b, Nan Wang ^{a,*}, Tetsuro Majima ^a, Lihua Zhu ^{a,*}

^a Key Laboratory of Material Chemistry for Energy Conversion and Storage, Ministry of Education, School of Chemistry and Chemical Engineering, Huazhong University of Science & Technology, Wuhan 430074, PR China

^b Hubei Key Laboratory of Resources and Ecological Environment Geology, Hubei Geological Bureau, Wuhan 430022, PR China



ARTICLE INFO

Keywords:

MnO₂
Oxygen vacancy
Mechanochemistry
Tetrabromobisphenol A
Peroxyomonosulfate

ABSTRACT

Oxygen vacancy (V_O) engineering can efficiently improve the catalytic activity of metal oxides. This work developed a solvent-free mechanochemical method to tailor V_O levels on the surface of commercial MnO₂ under ambient conditions. After a typical ball milling treatment at 350 rpm for 20 min, the obtained V_O -rich MnO₂ activated peroxyomonosulfate (PMS) to completely degrade tetrabromobisphenol (TBBPA) with a pseudo-first-order rate constant of 0.21 min⁻¹, being 22 times larger than that for non-milled MnO₂. ¹⁸O-labeling tests confirmed that singlet oxygen was generated from both PMS and lattice oxygen of MnO₂ as dominant active species for the TBBPA degradation. It was clarified that the catalytic activity of MnO₂ depends on not only V_O levels, but also the local environment of V_O , i.e., V_O -associated cations. The Mn⁴⁺/Mn³⁺ redox couple is more important than Mn³⁺/Mn²⁺, and V_O improves the oxygen mobility in/on MnO₂ and Mn⁴⁺/Mn³⁺ redox reactions for the activation of PMS.

1. Introduction

Advanced oxidation processes (AOPs) based on the generation of highly reactive oxygen species (ROSSs) such as singlet oxygen (1O_2), hydroxyl radical ($\bullet OH$), and sulfate radical anion (SO_4^{2-}) are effective for the removal of carcinogenic and mutagenic organic compounds in domestic and industrial wastewaters [1–5]. Compared to H₂O₂-mediated Fenton reactions used usually under acidic conditions, persulfate-based processes involving either peroxydisulfate (PDS) or peroxyomonosulfate (PMS) as oxidant have much attention due to a wider pH-working range [6,7]. As a transition metal species, Co²⁺ has been extensively studied for the activation of PMS [8,9]. Various heterogeneous cobalt-based catalysts such as cobalt oxides, Co-based mixed oxides, and cobalt hydroxide and its derivatives have been developed to activate PMS. However, leaching of Co²⁺ is not unavoidable, especially under acidic condition [10,11]. Therefore, much effort is devoted to develop Co-free heterogeneous catalysts to activate PMS.

Manganese is one of naturally abundant elements with low toxicity, and manganese oxides have more than 20 polymorphs. The multivalent nature and nonstoichiometric compositions make them more

complicated than simple metal oxides, and thus are considered as attractive candidates for the degradation of organic pollutants [12,13]. Wang's group studied a series of manganese oxides with different crystallographic phases, shapes, valence states, and metal doping for heterogeneous degradation of phenol in the presence of PMS [14–17]. They observed that α -MnO₂ showed higher activity than β - and γ -MnO₂ to activate PMS for the degradation of phenol due to higher oxygen mobility and more exposure of MnO₆ edges in α -MnO₂ than in β - and γ -MnO₂ [14]; they prepared Mn₂O₃ and Mn₃O₄ by calcinating MnO₂ at 550 °C and 950 °C in air, and found that the catalytic activity for the degradation of phenol decreases in the order of Mn₂O₃ > Mn₃O₄ > MnO₂, which relates to the oxidation state and oxygen mobility of manganese oxides [15]; they further found that Cu-doped (1 mol%) amorphous MnO₂ increased the degradation rate constant of phenol in the presence of PMS by 2.5 times than the un-doped MnO₂, because Cu-doping resulted in an increase for surface oxygen vacancies (V_O) from 0.78 to 0.79 and Mn⁴⁺/Mn³⁺ ratio from 1.4 to 1.9 [17]. Luo et al. employed a reflux method to synthesize cryptomelane typed MnO₂ containing Mn⁴⁺, Mn³⁺ and V_O , and found that this catalyst efficiently degraded organic dyes in the presence of PMS [18]. Biogenic manganese

* Corresponding authors.

E-mail addresses: nwang@hust.edu.cn (N. Wang), lhzh63@hust.edu.cn (L. Zhu).

oxide (BioMnO_x) was prepared from bacteria and Mn oxide to active PMS for degrading tetracycline three times faster than 3 dimensional $\alpha\text{-Mn}_2\text{O}_3$ due to the co-existence of Mn^{2+} , Mn^{3+} , and Mn^{4+} on the surface of BioMnO_x [19]. These studies demonstrate that the catalytic activity of manganese oxides is influenced by crystal structures, morphologies, surface area, chemical compositions, and oxidation states of Mn, in which the redox reactions of $\text{Mn}^{2+}/\text{Mn}^{3+}/\text{Mn}^{4+}$ and “oxygen mobility” of the lattice oxygen (O_L) are more important [20–22]. V_0 not only improves the release of surface O_L (O_{SL}) from the surface of manganese oxides, but also prompts the redox reactions of $\text{Mn}^{2+}/\text{Mn}^{3+}/\text{Mn}^{4+}$. In addition, V_0 bears higher electron density to facilitate the dissociation of H_2O_2 into $\bullet\text{OH}$ [15,18]. Thus, V_0 increases the catalytic activity of manganese oxides.

The fabrication of V_0 in metal oxides includes two approaches: (i) substitution by metallic ions with lower valence states and similar ionic radius; (ii) partial reduction of metal oxides at high temperatures under reducing environments [23–26]. Comparably, the latter approach is of particular interest due to the morphological compatibility between two different metallic ions of the same element. Nevertheless, the annealing raises the growth of particles and decreases the surface area, thereby reducing the catalytic activity of manganese oxides.

The mechanochemical route is a robust, green and low-cost method for preparing various functional nanomaterials by ball milling [27,28], because it is conducted in a solid state at modest temperatures and pressures and is easily scaled up without the usage of solvents. During ball milling, high impact and collisions between balls not only initiate the rotation, rupture, and reformation of chemical bonds, but also produce fresh and larger surfaces by fracturing material particles [29]. For example, Amrute et al. reported that the ball milling of $\gamma\text{-AlO(OH)}$ yields nm-sized $\alpha\text{-Al}_2\text{O}_3$ with a surface area of $140 \text{ m}^2 \text{ g}^{-1}$, being much higher than that ($10 \text{ m}^2 \text{ g}^{-1}$) for $\alpha\text{-Al}_2\text{O}_3$ prepared by the pyrolysis [30]. As we know, the ball milling of metal oxides (such as CaO , MgO , Al_2O_3 , and MnO_2) produces V_0 , trapped electrons (e^-_{tr}) and active oxygen from losing O_{SL} , which, as reactive species, may contribute to the reductive or oxidative degradation of organic pollutants [22,31–33]. This inspires us to tailor V_0 degrees on the surface of MnO_2 by ball milling.

In the present study, we succeeded to mechanochemically tailor V_0 level on the surface of MnO_2 by ball milling commercial MnO_2 . The obtained V_0 -rich MnO_2 was employed as a catalyst to degrade tetrabromobisphenol A (TBBPA), a compound widely used as brominated flame retardant in plastic additives, wire brushes, and circuit boards, in the presence of PMS. It was found that the V_0 tailoring significantly increased the catalytic activity of MnO_2 . The catalytic activity of MnO_2 was experimentally correlated with its V_0 level, and the roles of V_0 for the ROSs generation and the TBBPA degradation mechanism on V_0 -rich MnO_2 were discussed.

2. Materials and methods

2.1. Materials

Manganese dioxide ($\gamma\text{-MnO}_2$, 91%), ethanol (99.7%), tert-butyl alcohol (TBA, ≥ 99%), and sodium thiosulfate pentahydrate ($\text{Na}_2\text{S}_2\text{O}_3 \cdot 5\text{H}_2\text{O}$, ≥ 99.0%) were obtained from Sinopharm Chemical Reagent (Shanghai, China). PMS (2KHSO₅-KHSO₄-K₂SO₄, 4.7% active oxygen) was purchased from Shanghai D&R Finechem (Shanghai, China). NaOH, HNO₃, KI, NaHCO₃, were obtained from Taixing Chemical (Tianjin, China). TBBPA ($\text{C}_{15}\text{H}_{12}\text{Br}_4\text{O}_2$), obtained from Aladdin Chemistry (Shanghai, China), was dissolved (0.4 mg) in 100 mL of 0.1 M NaOH solution to prepare a stock solution (4 g L⁻¹). Phenol ($\text{C}_6\text{H}_5\text{OH}$), β -carotene, chloroform (CHCl_3 , 98%), 5,5-dimethyl-1-pyrroline-N-oxide (DMPO), and 2,2,6,6-tetramethylpiperidine (TEMP) were obtained from Sigma-Aldrich (St. Louis, USA). Double distilled water was used in this work. All chemicals were analytical reagents and used as received without further purification.

2.2. Mechanochemically tailoring MnO_2 and characterizations

A series of MnO_2 samples with different levels of V_0 were synthesized by ball milling commercial MnO_2 . Briefly, 4 g MnO_2 was placed into a zirconia jar with 50 zirconia balls at a ball-to-sample mass ratio of 22:1. The jar was tightly closed and well-fixed in the grinding chamber of the planetary ball mill (YXQM-4 L MITR, China). The rotation speed of the planetary disk was set at 350 rpm with automatic rotation direction changing per 15 min. After a certain time, interval, the ball milling was stopped, and the milled mixture was collected and stored at room temperature. The tuning of V_0 levels was first conducted by changing the rotation speed from 100 to 380 rpm, which confirmed the highest V_0 -rich MnO_2 was prepared at 350 rpm. Then, the tuning of V_0 levels was conducted at 350 rpm by changing ball milling time (t_{bm}) from 2 to 30 min. The MnO_2 sample obtained by ball milling commercial MnO_2 at 350 rpm for time t was referred to as $\text{bm}_t\text{-MnO}_2$. For example, commercial MnO_2 without ball milling ($t = 0$) was named as $\text{bm}_0\text{-MnO}_2$ for convenience, and the MnO_2 sample obtained by ball milling commercial MnO_2 at 350 rpm for 20 min was named $\text{bm}_{20}\text{-MnO}_2$.

The speciation analysis of Mn element in the bulk MnO_2 before and after mechanochemical treatments was analyzed based on the determination of Mn ions at different valence states by using the selective dissolution according to the previous method [20]. The detailed experimental information was shown in [Section S1 of Supporting Information \(SI\)](#). The surface morphology of the catalysts was characterized on an FEI Technai G2 F30 transmission electron microscopic (TEM) instrument. XRD patterns were obtained on a Bruker D8 advance diffractometer using filtered Cu K α radiation source, with accelerating voltage 40 kV and current 40 mA. The element composition and chemical oxidation state were investigated by X-ray photoelectron spectra (XPS) on a TM K-Alpha spectrometer (Thermo Scientific TM) with Al K α radiation as the exciting source (300 W). Binding energies were calibrated versus the carbon signal at 284.6 eV. Raman spectra were recorded on a Renishaw inVia Reflex Raman spectrometer with 488 nm laser excitation. EPR spectra of catalysts powders were performed on an EPR spectrometer (JEOL, JES-X320). N_2 adsorption/desorption was measured using an ASAP 2020 to obtain pore volume and the BET specific surface area. Prior to the measurements, samples were degassed at 120 °C under vacuum for 5 h. The temperature-programmed desorption of O_2 ($\text{O}_2\text{-TPD}$) was conducted on AMI-300 chemisorption analyzer according to the previous procedure with modifications [34]. In each run, 100 mg MnO_2 was purged with Ar (30 mL min⁻¹) at 110 °C for 1 h. After cooling down to 50 °C, the residual material was treated by the flow of 10% O_2 in He (30 mL min⁻¹) for 1 h and then purged successively by He flow (30 mL min⁻¹) for 0.5 h. Finally, the material was purged with He and heated from 50° to 850°C at a rate of 10 °C min⁻¹, and kept at 850 °C for 0.5 h. The release of O_2 was monitored with a thermal conductivity detector (TCD).

The redox reactions on the surface of MnO_2 were studied by cyclic voltammetry with a three electrode system composed of MnO_2 -loaded glass carbon electrode ($\text{MnO}_2\text{/GCE}$) as working electrode, a platinum wire as an auxiliary electrode, and Ag/AgCl as a reference electrode. The CV curves were recorded in an O_2 -free Na_2SO_4 solution (0.5 M) as the electrolyte with a potential window range from -0.8 to 1.2 V. Prior to use, GCE was polished on chamois leather with alumina slurry, washed successively with ethanol and deionized water under ultrasonic irradiation for 5 min, and dried at 60 °C. To fabricate MnO_2 -loaded working electrode, 2 mg MnO_2 was dissolved in 1 mL ethanol containing 0.1 wt% Nafion and subjected to sonication for 1 h. Thereafter, 20 μL of the formed MnO_2 ink was coated onto the GCE and dried at room temperature. With the similar three electrode system, the open-circuit potentials of $\text{MnO}_2\text{/GCE}$ in Na_2SO_4 solution were monitored. When PMS and/or TBBPA was present in Na_2SO_4 solution, the solution pH was adjusted to pH 8.0 by using diluted H_2SO_4 and/or NaOH.

2.3. Degradation experiments and analysis

TBBPA degradation experiments were conducted in a 100 mL-beaker containing TBBPA solution, MnO_2 , and PMS at pH 8 under magnetic stirring in a water bath at 30 °C. In a typical run, 15 mg MnO_2 was added to 50 mL TBBPA solution (40 mg L^{-1}). After 30 min for allowing the adsorption-desorption equilibrium of TBBPA on MnO_2 , the TBBPA degradation was initiated by rapidly adding 100 μL PMS (50 g L^{-1}). At given time intervals, 2 mL of sample was taken and immediately mixed with 100 μL $\text{Na}_2\text{S}_2\text{O}_3$ (0.5 mol L^{-1}) as a quencher to stop the degradation. After separating solid mixture by a 10 min centrifugation at 14,000 rpm, the residual solution was filtered through a 0.22 μm membrane and the absorbance at 310 nm was measured with a Cary 60 UV-vis spectrophotometer. PMS concentration was evaluated using an iodometric process following the previous report with modifications [17]. At given time intervals, 1 mL reaction solution was taken, filtered through a 0.22 μm membrane, and mixed with 1 mL aqueous solution containing KI (0.5 mol L^{-1}) and NaHCO_3 (0.07 mol L^{-1}). After 3 min, 1 mL of the above solution was diluted by 1 mL water and then measured at 352 nm on a Cary 60 UV-vis spectrophotometer.

The TBBPA degradation products were identified on a Waters Acquity ultra performance liquid chromatography (UPLC) coupled with a Waters Xevo TQ-S tandem quadrupole mass spectrometer (MS). An isocratic mode with acetonitrile-aqueous solution (85:15, v/v) at 0.3 mL

min^{-1} as mobile phase was employed to separate the components on a C18 column ($1.7 \mu\text{m}$, $2.1 \times 100 \text{ mm}$). Mass spectrometry with electrospray ionization (ESI) source was operated in negatively charged mode. The total organic carbon (TOC) was measured with a TOC-analyzer (TOC-L CPH, Shimadzu, Japan). Adducts of ROS with DMPO or TEMP as spin trapping reagents were measured on a Bruker EMX-nano EPR instrument. The leached Mn ions in degradation solution were detected by inductively coupled plasma-atomic emission spectrometry (ICP-AES; Thermo Fisher iCAP7200 Plus).

The reusability and stability of catalyst was checked for the 5 successive degradation cycles of TBBPA in MnO_2/PMS under air and nitrogen atmosphere. After each degradation run, MnO_2 was collected by filtration, washed with ethanol to remove possible degradation products adsorbed on the catalysts and then dried at 60 °C. The recovered MnO_2 was dispersed into fresh TBBPA solution, followed by adding PMS to initiate the degradation reaction.

2.4. DFT computational methodology

To give further insight into the role of V_0 on the catalytic activity of MnO_2 , density functional theory (DFT) calculations were conducted based on the Vienna Ab-initio Simulation Package (VASP) [35–37]. The electron-ion interactions were described by the Projected Augmented-Wave (PAW) potentials, while the exchange-correlation

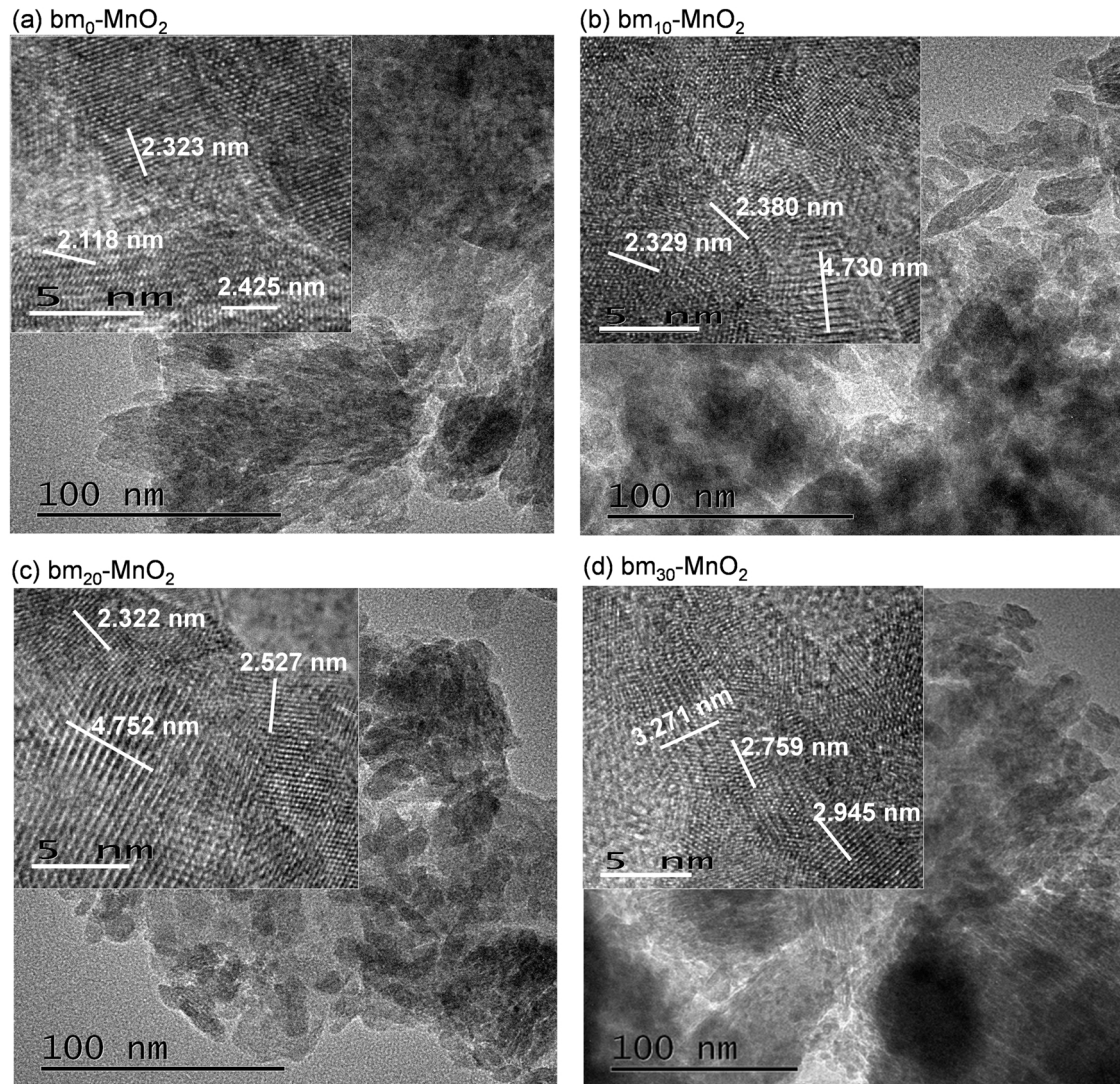


Fig. 1. TEM images of $\text{bm}_0\text{-MnO}_2$ (a) and $\text{bm}_t\text{-MnO}_2$ (b–d) prepared with ball milling time of 10 min (b), 20 min (c), and 30 min (d).

interactions were calculated by employing the Perdew-Burke-Ernzerhof (PBE) pseudopotentials of Generalized Gradient Approximation (GGA) [38–41]. The vdW-D3 method developed by Grimme was employed to describe the van der Waals interaction [42]. The detailed information was described in Section S2.

3. Results and discussion

3.1. Characterizations of V_O -rich MnO_2

Fig. 1 showed TEM images of commercial γ - MnO_2 before and after ball milling. Both commercial (non-milled; bm_0) and milled (bm_t) MnO_2 were composed of irregularly shaped plates with stacking, and the ball milling led to the formation of nuts-like forms scattered on the surface of plates, especially in the edge region. The high-resolution TEM (HRTEM) images (the insert in **Fig. 1**) showed that bm_0 - MnO_2 exhibited several kinds of parallel planes with the interplanar distance of 0.21, 0.23 and 0.24 nm corresponding to (300) (230) and (131) planes of γ - MnO_2 , respectively [43], together with several unclear planar fringes such as on (120) facet with a theoretical interplanar distance of 0.40 nm [44]. After ball milling, the interplanar space of (300), (230) and/or (131), and (120) facet increased to 0.23–0.25, 0.24–0.29, and 0.46–0.48 nm, respectively. These results suggested that ball milling increases the interplanar distance of MnO_2 .

Fig. 2a showed XRD patterns of MnO_2 before and after milling. For bm_0 - MnO_2 , four peaks were observed at 2θ of 22°, 37.2°, 42.5°, and 56.3°, being indexed to (120), (131), (300), and (160) γ - MnO_2 , respectively, according to JPCDS card No 14-0644 [45]. After a ball milling treatment, there were no observed changes in XRD patterns, suggesting no changes for the crystalline structure of γ - MnO_2 . **Fig. 2b** illustrated the N_2 adsorption/desorption isotherms. All MnO_2 showed the type-IV

isotherms with a substantial H3-type hysteresis loop, suggesting the presence of mesopores in the structure of MnO_2 . **Fig. 2c** showed the pore size distribution determined by BJH method. bm_0 - MnO_2 consists of a distribution of mesopores with pore radia between 10 and 100 nm with a dominant pore size near 19 nm. As t_{bm} was increased from 0 to 30 min, the content of pores with radia around 19 nm decreased by 43–56%, and those with radia of 25–100 nm increased, suggesting that the ball milling treatment increases the pore size of γ - MnO_2 . The pore volume increased from 0.039 to 0.16 $cm^3 g^{-1}$ for bm_{20} - MnO_2 , and decreased to 0.13 $cm^3 g^{-1}$ for bm_{30} - MnO_2 . The BET specific surface areas were measured to be 28.8, 29.5, 35.7, 38.1, and 42.6 $m^2 g^{-1}$ for bm_0 - MnO_2 , bm_5 - MnO_2 , bm_{10} - MnO_2 , bm_{20} - MnO_2 , and bm_{30} - MnO_2 , respectively (inset of **Fig. 2b**). The origin of the gradual improvement of these textural properties was expected from the particle size reduction induced by mechanical force during ball milling for different time [29]. The increased specific surface area along with larger pore-size and pore-volume may offer more active sites and easier accessibility for the diffusion and activation of PMS on MnO_2 .

Mn element speciation analysis was conducted for the bulk of bm_0 - MnO_2 and bm_t - MnO_2 (**Fig. 2d**). The sample of bm_0 - MnO_2 showed the co-existence of Mn^{4+} and Mn^{3+} with 76.3% and 23.7%, respectively, consisting with the commonly observed [22,46,47]. The ball milling decreased the content of Mn^{4+} and increased the contents of Mn^{3+} and Mn^{2+} . For example, after ball milling for 5 min, the contents (atomic percentages) of Mn^{4+} , Mn^{3+} and Mn^{2+} became 73.5%, 24.8%, and 1.7%. As the milling time was further increased to 30 min, the content of Mn^{4+} decreased to 69.9%, while that of Mn^{3+} and Mn^{2+} increased to 26.6% and 3.5%, respectively. During ball milling, the high impact and collision between balls can induce losing O_{SL} of metal oxides such as CaO , Al_2O_3 , and MnO_2 , resulting in the formation of oxygen atom (O^*), V_O and two e^-_{tr} [22,31,48]. The e^-_{tr} at V_O sites reduce Mn^{4+} and Mn^{3+} to

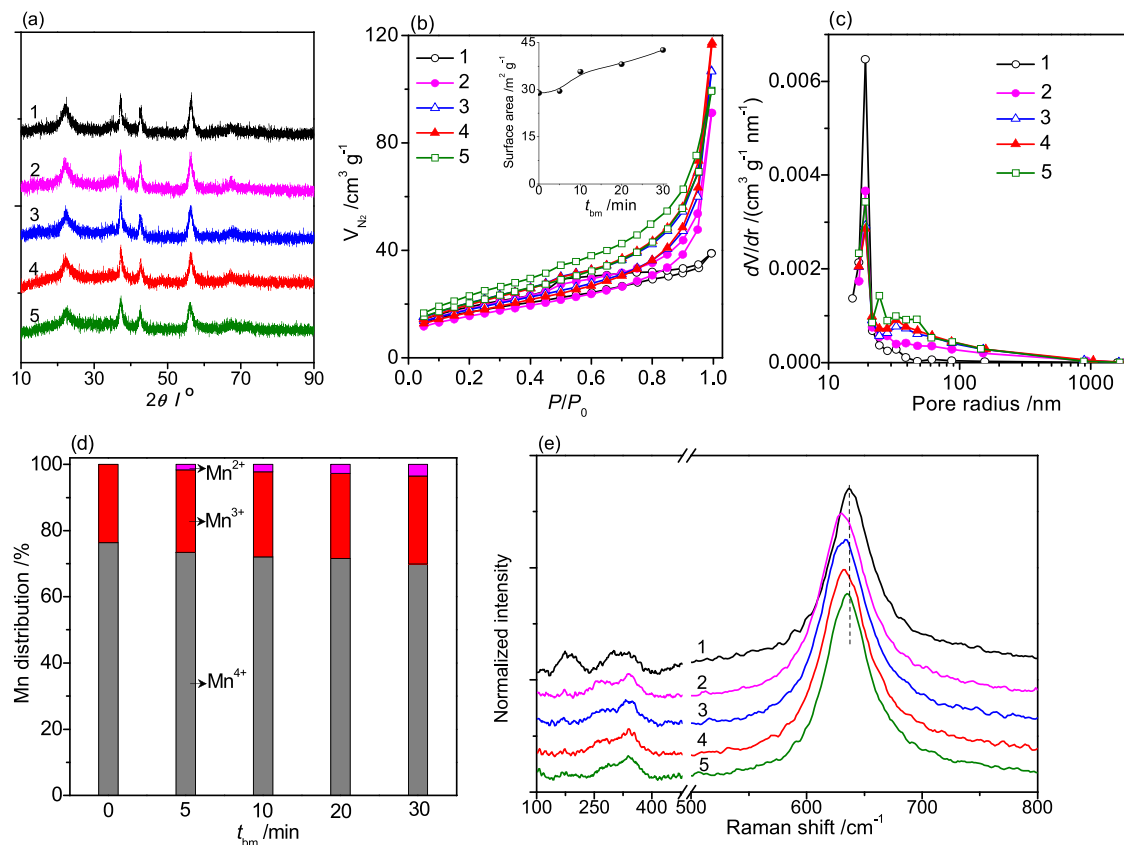


Fig. 2. XRD patterns (a), N_2 adsorption isotherms (b), pore size distribution (c), bulk distribution of Mn^{x+} (d) and Raman spectra (e) for bm_0 - MnO_2 (1) and bm_t - MnO_2 (2–5) synthesized by ball milling MnO_2 for time of 5 min (2), 10 min (3), 20 min (4), and 30 min (5). The inset in (b) was the BET surface areas of the related samples.

yield Mn³⁺ and Mn²⁺, respectively. Since MnO₂ is composed of Mn and O, the atomic ratio of O/Mn (without involvement of physically adsorbed water) in bulk MnO₂ was calculated according to the charge balance theory [22]. The atomic ratio of O/Mn was found to decrease from 1.88 to 1.85 with increasing the milling time from 0 to 30 min, suggesting an increase in the ratio of V_O to O_L (V_O/O_L) from 6.3% to 9.2% (Fig. S1).

Raman spectra further reveal the mechanochemical treatment disrupted Mn–O–Mn chains of γ -MnO₂. The as-received γ -MnO₂ showed three bands near 180, 320 and 637 cm⁻¹, corresponding to the external vibration of the [MnO₆] octahedral, the Mn–O bending vibrations ($\beta_{\text{Mn–O}}$) and the Mn–O stretching vibrations ($\nu_{\text{Mn–O}}$), respectively [49]. After ball milling for 5–30 min, the band near 180 cm⁻¹ significantly decreased, suggesting the loss of some surface oxygen. The band near 320 cm⁻¹ split into two bands at 264 and 360 cm⁻¹, indicating two distinct local environments of Mn–O [50]. The band near 637 cm⁻¹ moved to 630–634 cm⁻¹, suggesting the weakening and/or elongation of Mn–O bond [51].

3.2. Catalytic activity of mechanochemically tailored V_O-rich MnO₂

TBBPA was chosen as a model pollutant to evaluate the catalytic activity of bm_t-MnO₂ in the presence of PMS (bm_t-MnO₂/PMS). All the added TBBPA disappeared completely in bm₂₀-MnO₂/PMS after 20 min, while it decreased by 30% in bm₀-MnO₂/PMS (curves 1 and 2 in Fig. 3a).

As the control tests (curves 3 and 4 in Fig. 3a), the TBBPA degradation yield was less than 10% for either bm₂₀-MnO₂ or PMS even after 60 min. The TBBPA degradation followed a pseudo-first-order reaction kinetics with $\ln(c/c_0) = -kt + \text{constant}$ (Fig. 3d), where c_0 and c are the TBBPA concentrations (mg L⁻¹) at reaction time of 0 and t (min), respectively, and k is the pseudo-first-order rate constant (min⁻¹). The value of k was calculated to be 0.21 min⁻¹ for bm₂₀-MnO₂/PMS, being 22, 105, and 191 times larger than those for bm₀-MnO₂/PMS (0.0097 min⁻¹), PMS (0.0020 min⁻¹), and bm₂₀-MnO₂ (0.0011 min⁻¹), respectively. This indicates that both bm₀- and bm₂₀-MnO₂ can activate PMS for the TBBPA degradation, and bm₂₀-MnO₂ has 22-time higher catalytic activity than bm₀-MnO₂ to degrade TBBPA in the presence of PMS.

The degradation products of TBBPA in bm₂₀-MnO₂/PMS were analyzed by UPLC-MS measurement in the negative ionization mode. The total ion current (TIC) chromatogram of the sample before adding PMS showed one component at retention time of 7.25 min with mass fragment ions at m/z 539/541/543/545/547 with an isotopic ratio of 1:4:6:4:1, which is assigned to TBBPA (Fig. S2). After the degradation in bm₂₀-MnO₂/PMS for 2–5 min, several new and broad peaks were observed at retention time of 0.9–1.5 min with low separation efficiency (Fig. S2), suggesting that the degradation products possess high polarities because of their poor retention on C18 column. These peaks possessed similar fragment ions at m/z 383/385, 247/249/251, 113/115, and 80 (Figs. S3–S8), which may be assigned to bromoalkenes with

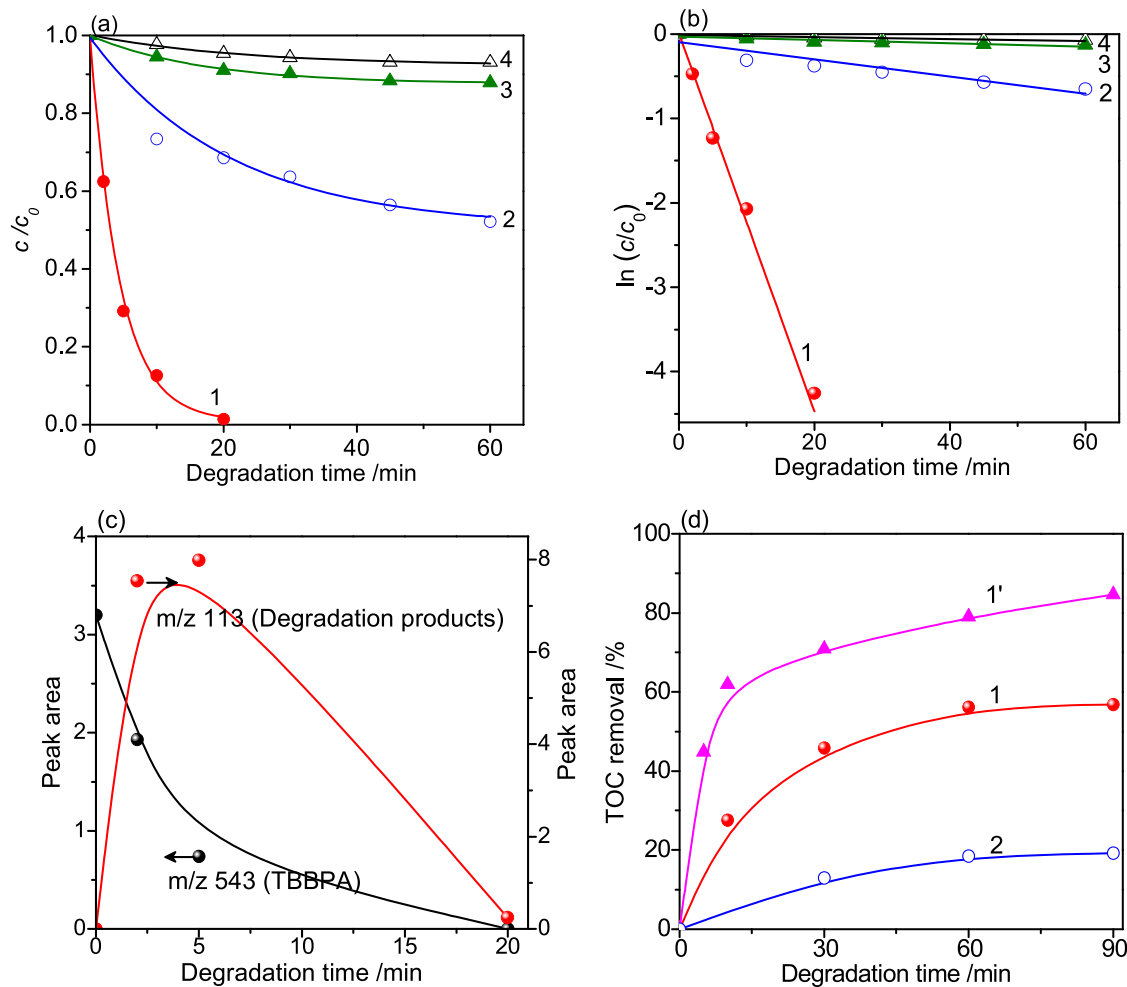


Fig. 3. Degradation of TBBPA (40 mg L⁻¹) (a) and its kinetics (b) in bm₂₀-MnO₂/PMS (1), bm₀-MnO₂/PMS (2), PMS (3), and bm₂₀-MnO₂ (4). Profiles of TBBPA residual and its degradation intermediates accumulation in bm₂₀-MnO₂/PMS (c). The concentrations of TBBPA residual and its degradation intermediates were expressed respectively by the peak areas of the extracted ions with m/z 543 and 113 in the MS spectra. TOC removal (d) for the degradation of TBBPA in systems of bm₂₀-MnO₂/PMS (1), bm₀-MnO₂/PMS (2) and bm₂₀-MnO₂ + 0.3 g L⁻¹ PMS (1'). Unless otherwise stated, the basic degradation reaction conditions were as follows: catalysts loading, 0.3 g L⁻¹; PMS addition, 0.1 g L⁻¹; solution pH of 8 after adding PMS; 30 °C.

the molecular formula of $C_{10}H_8Br_2O_6$ and the structure like 2,4-dibromo-3-hydroxy-7-oxodeca-2,4,8-trienedioic acid, 8,10-dibromo-5,9-dihydroxy-4,10-dioxodeca-2,6,8-trienoic acid, and/or their isomers. After the degradation for 20 min, TBBPA and the above mentioned degradation products decreased to zero (Figs. 3c, and S2–S6). This is in agreement with the changes of UV-vis absorption spectra for TBBPA before and after degradation in bm_{20} -MnO₂/PMS. After degradation for 20 min, the absorption of degradation solution in 250–350 nm significantly decreased to 0 without any new peak over 230 nm (Fig. S9), indicating no formation of aromatic or conjugated-triene products. The removal of total organic carbon (TOC) reached 57% at 90 min, being 3 times larger than that (19%) for bm_0 -MnO₂/PMS. It was noted that the removal of TOC in both systems became slower at the latter reaction stage ranging from 30 to 90 min. No residual PMS was detectable in bm_{20} -MnO₂/PMS/TBBPA after degradation for 20 min, while the residual of PMS was 76.2% in bm_0 -MnO₂/PMS/TBBPA (Fig. S10a). In the control tests, the decomposition of PMS in TBBPA-free MnO₂/PMS was slower than in the presence of TBBPA (Fig. S10a and b). This suggests that the consumption of ROSs by TBBPA accelerated the decomposition of PMS, and the slower TOC removing in bm_0 -MnO₂/PMS/TBBPA at the latter stage was attributed to the complete decomposition of PMS. This proposal was further supported by the fact that the removal of TOC in bm_{20} -MnO₂/PMS increased to 85% at 90 min when the addition of PMS was increased from 0.1 to 0.3 g L⁻¹ (Fig. 3d).

Effects of rotation speed and ball milling time on the catalytic activity of bm_t -MnO₂ were studied. A series of MnO₂ samples were prepared by ball milling for 5 min at various rotation speed. As the rotation speed was increased from 100 to 380 rpm, the k value of the TBBPA degradation increased from 0.0097 at 100 rpm to 0.049 min⁻¹ at 350 rpm, and then almost kept unchanged (Fig. 4a). At 350 rpm, other series of MnO₂ samples were prepared with changing ball milling time t_{bm} . As t_{bm} was increased from 0 to 20 min, k increased from 0.0097 to 0.21 min⁻¹ (Fig. 4b). A further increase of t_{bm} to 30 min, k decreased to 0.13 min⁻¹. This suggests that a mechanochemical treatment via ball milling commercial γ -MnO₂ can enhance the catalytic activity of MnO₂, and a moderate t_{bm} of 20 min at 350 rpm was recommended to obtain MnO₂ with the best catalytic activity. The present method was also used to treat other four available commercial β -MnO₂ as named as S1–S4 for convenient. For as-received S1 and S2 MnO₂ with nearly the same activity as γ -MnO₂, a 20-min ball milling treatment at 350 rpm improved k of the TBBPA degradation by 18–19 times, while k was increased by 8 times for S3 and S4 MnO₂ having 4–5 times higher activity than γ -MnO₂ (Fig. S11). This suggests that the present mechanochemical method is efficient to improve the catalytic activity of various MnO₂.

The catalytic activity of bm_{20} -MnO₂ for the degradation of TBBPA in the presence of PMS was also influenced by degradation conditions. For example, as bm_{20} -MnO₂ loading was increased from 0 to 0.5 g L⁻¹, k

increased first and then kept almost constantly (Fig. S12a). A similar trend was observed for the dependence of k on the initial concentration of PMS (0–0.2 g L⁻¹) (Fig. S12b). As solution pH was increased from 8 to 12, k decreased with a linear relationship between $\ln k$ and $\ln[H^+]$ (Fig. S12c and d), due to that H⁺ involves in the redox reactions of Mn⁴⁺/Mn³⁺ and Mn³⁺/Mn²⁺ as well as influences species distribution of PMS [52,53]. As temperature was increased from 20 to 50 °C at pH 8, k in bm_{20} -MnO₂/PMS increased from 0.14 to 0.43 min⁻¹, each of which is higher than that in bm_0 -MnO₂/PMS at the same given temperature (Fig. 4c). According to the Arrhenius equation, the apparent activation energy (E_a) and pre-exponential factor (A_{app}) are calculated to be 28.5 kJ mol⁻¹ and 1.6×10^4 min⁻¹ in bm_{20} -MnO₂/PMS (insert of Fig. 4c). Compared with bm_0 -MnO₂/PMS ($A_{app} = 8.9 \times 10^5$ min⁻¹; $E_a = 46.1$ kJ mol⁻¹), the smaller A_{app} in bm_{20} -MnO₂/PMS would decrease k by 55.6 times, but the smaller E_a for bm_{20} -MnO₂ would increase k by $(0.68\text{--}1.3) \times 10^3$ times in 20–50 °C. Thus, it can be concluded that the decreased E_a causes bm_{20} -MnO₂ to show higher catalytic activity than bm_0 -MnO₂.

In order to evaluate the activity level, bm_{20} -MnO₂/PMS was also employed to degrade phenol, since many studies have employed MnO₂ or its composites to degrade phenol but not TBBPA [14,15,17,54–57]. In the presence of 0.2 g L⁻¹ bm_{20} -MnO₂ and 0.1 g L⁻¹ PMS, all the added phenol (20 mg L⁻¹) was completely degraded in 25 min at 25 °C with k of 0.22 min⁻¹, being 10.5 times higher than that using bm_0 -MnO₂ (Fig. S13, and Table S1). Compared with most of reported MnO₂ or its composites (Table S1), bm_{20} -MnO₂ exhibits 1.2–8.8 times higher activity and consequently permits a much decreased requirements of PMS addition by 4–20 times.

It is known that the ball milling treatment increases the BET surface area of MnO₂ (Fig. 2b), probably resulting in activating PMS efficiently. When k is normalized with the surface area of MnO₂ (i.e., BET surface area × mass), the obtained specific activity per surface area (k' min⁻¹ m⁻²) will be independent on t_{bm} , if the BET surface area is the key factor in determining the activity of MnO₂. However, k' increased from 0.023 min⁻¹ m⁻² at $t_{bm} = 0$ –0.38 min⁻¹ m⁻² at $t_{bm} = 20$ min, and then decreased to 0.20 min⁻¹ m⁻² at $t_{bm} = 30$ min (Fig. S14). This means that the contribution of BET surface area is not so important in the present work. The reason for the enhanced catalytic activity of mechanochemically tailored MnO₂ will be discussed as below.

3.3. Mechanochemically tailoring levels and local chemical environments of V_O

Since the activation reactions of PMS occur on the surface of MnO₂, the surface chemical compositions of MnO₂ before and after ball milling were analyzed by XPS. Both non-milled and milled MnO₂ showed characteristic XPS signals of O (e.g., near 24.3 and 531 eV for O 2 s and

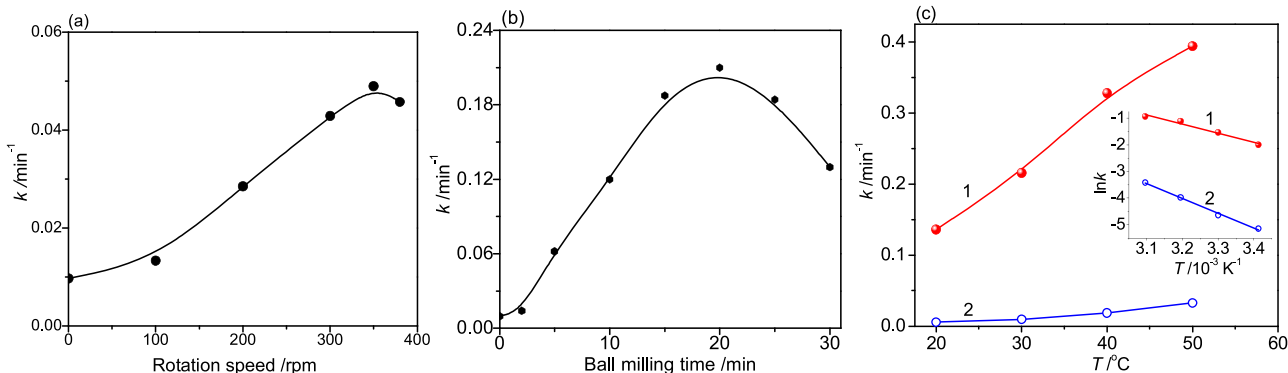


Fig. 4. Effects of rotation speed (a) and ball milling time (b) on the pseudo-first-order rate constant (k) of the TBBPA degradation in bm_t -MnO₂/PMS. Rotation speed and ball milling time were fixed at 5 min and 350 rpm in (a) and (b), respectively. Effect of temperature on k of the TBBPA degradation (c) in bm_{20} -MnO₂/PMS (1) and bm_0 -MnO₂/PMS (2). Inset of (c) is Arrhenius plots for $\ln k$ vs. T^{-1} .

1 s, respectively) and Mn (e.g., 82–88 and 640–655 eV for Mn 3 s and 2p, respectively) together with inevitable carbon contaminations at 284.8 eV (Fig. S15a). The high-resolution XPS spectra of O 1s contained three components at 529.8, 531.1, and 532.1 eV (Fig. S16a), which was assigned to O_{SL}, chemically adsorbed oxygen (O_{c-ads}, e.g., O²⁻, O⁻, or OH groups) near V_O, and physically adsorbed water, respectively. Since chemically adsorbed oxygen represents the amount of V_O, the ratio of V_O/O_{SL} can be calculated from the ratio of peak area for the component of O_{c-ads} to that of O_{SL}. As the ball milling time increased from 0 to 25 then to 30 min, the V_O/O_{SL} ratio increased from 0.194 to 0.326 at 25 min, and then decreased to 0.306 at 30 min (Table 1), suggesting that 25 min was the best selection of the milling time for producing V_O on the surface of MnO₂.

Mn element speciation analysis in the bulk of MnO₂ showed that a ball milling treatment caused the conversions of Mn⁴⁺ to Mn³⁺ and Mn²⁺. XPS analysis was employed to study Mn^{x+} distribution on the surface of bm₀-MnO₂ and bm_t-MnO₂. The high-resolution XPS Mn 2p spectra of all the samples contained two spin-orbit splitting components near 643 and 653 eV for 2p_{3/2} and 2p_{1/2}, respectively (Fig. S15b). Since both the two components provide the same chemical information, only Mn 2p_{3/2} peak with stronger intensity was deconvoluted as shown in Fig. S16b and Table 1. For bm₀-MnO₂, two components appeared around 642.5 and 643.8 eV with percentages of 54.3% and 45.7% corresponding to Mn³⁺ and Mn⁴⁺, respectively, and the ratio of Mn³⁺ was higher than that (23.7%) in the bulk of MnO₂. This suggests that the V_O mainly exists on the surface of MnO₂ as commonly observed [22,46,47]. After a pretreatment by ball milling for 2 min, the percentage of Mn⁴⁺ decreased to 34.3%, and that of Mn³⁺ increased to 62.2%, and a new peak corresponding to Mn²⁺ appeared at 641.4 eV with a percentage of 3.5%. As the ball milling time was increased from 2 to 30 min, the percentage of Mn³⁺ decreased to 57.9% at 25 min and then increased to 58.9% at 30 min, the Mn²⁺ content increased firstly to 8.9% at 25 min and then decreased to 6.7% at 30 min. The change of the Mn⁴⁺ percentage was complex and fluctuated between 32.9% and 34.7%. This is because that the ball milling probably promoted the release/regeneration of O_{SL} and multiple redox reactions of Mn^{4+/3+/2+}. The percentages of Mn⁴⁺, Mn³⁺ and Mn²⁺ depended on their consumption and generation rates.

Pristine γ-MnO₂ is composed of disordered 1 × 1 and 1 × 2 tunnels made up of edge-shared [Mn₆O₆] octahedral unit. Each Mn⁴⁺ is coordinated by six O²⁻ (named as O-Mn⁴⁺-O₅ (Mn_(A)), while each O²⁻ is coordinated by three Mn⁴⁺ (named as Mn⁴⁺-O-(Mn⁴⁺)₂ (O_(A))). The

speciation analysis of Mn and O confirmed the coexistence of Mn⁴⁺, Mn³⁺, O²⁻ and V_O on the surface of bm₀-MnO₂, but without Mn²⁺. Based on the atomic ratio of Mn⁴⁺: Mn³⁺: Mn²⁺, the average number of V_O (*n*_{V_O}, avg) associated with one Mn ion on the surface of bm₀-MnO₂ was calculated to be 0.81. In terms of V_O number (*n*_{V_O}) for any given Mn atom, there are two possible types of Mn⁴⁺ ions with *n*_{V_O} = 0 and 1 (Mn_(A) and Mn_(B)) and one type of Mn³⁺ with *n*_{V_O} = 1 (Mn_(C)) (Scheme 1a). In terms of valance state of Mn ions, both lattice oxygen and V_O have four possible types (i.e., Mn⁴⁺ number of 3, 2, 1 and 0 for O_(A) (V_{O(A)}), O_(B) (V_{O(B)}), O_(C) (V_{O(C)}) and O_(D) (V_{O(D)}), respectively) (Scheme 1b). The mechanochemical tailoring treatment, in general, increased the level of V_O on the surface of MnO₂; the calculated *n*_{V_O}, avg of the tailored MnO₂ increased from 0.94 to 1.15 as *t*_{bm} was increased from 2 to 25 min. This suggests that the high impact and collisions between balls promotes the breakage of some Mn-O to generate V_O and 2e⁻_{tr}, and consequently the reduction of two Mn ions would occur to maintain the charge balance (Scheme 1a). Since Mn³⁺ possesses a larger radius and less positive charges than Mn⁴⁺, the lattice expansion and the deficient charge make oxygen ions in the vicinity of Mn³⁺ be easy to release, producing V_O in an increasing order of O_(D) > O_(C) > O_(B) > O_(A) (Scheme 1b). The presence of V_O brings unbalanced charge to its neighboring Mn ions (Scheme 1a). The excessive positive charge of Mn⁴⁺ and Mn³⁺ in Mn_(B), Mn_(D) and Mn_(E) favors their reduction by e⁻_{tr} to generate Mn³⁺ and Mn²⁺, respectively. On the contrast, the positive charge of Mn²⁺ in Mn_(F) is deficient, thereby preferring to react with neighboring Mn⁴⁺ to generate Mn³⁺ species (Scheme 1a). This indicates that Mn²⁺ and Mn⁴⁺ cannot coordinate with the same V_O and oxygen ion. Thus, there may be six types of Mn ions (i.e., Mn_(A-F)) and five types of V_O (i.e., V_{O(A-E)}) on the surface of mechanochemically tailored MnO₂ (Scheme 1a and b). An increase in V_O, Mn³⁺ and/or Mn²⁺ causes a larger lattice distortion and less favorable coordination for Mn⁴⁺. Consequently, some V_O tend to be filled by adsorbed oxygen to maintain the local charge balance and the stable coordination of Mn⁴⁺, e.g., the conversion of V_{O(E)} and V_{O(C)} to O_(B) and O_(A), respectively (Scheme 1b). This is the reason why the ratio of Mn⁴⁺ fluctuated during the mechanochemical treatment (Table 1). Thus, it can be concluded that the mechanochemical treatment not only increases V_O levels, but also changes the local chemical environments of V_O, i.e., the distribution of V_O-associated Mn ions. Such changes may influence the catalytic activity of MnO₂.

3.4. Confirmation of the dominant effect of V_O on the catalytic activity of MnO₂

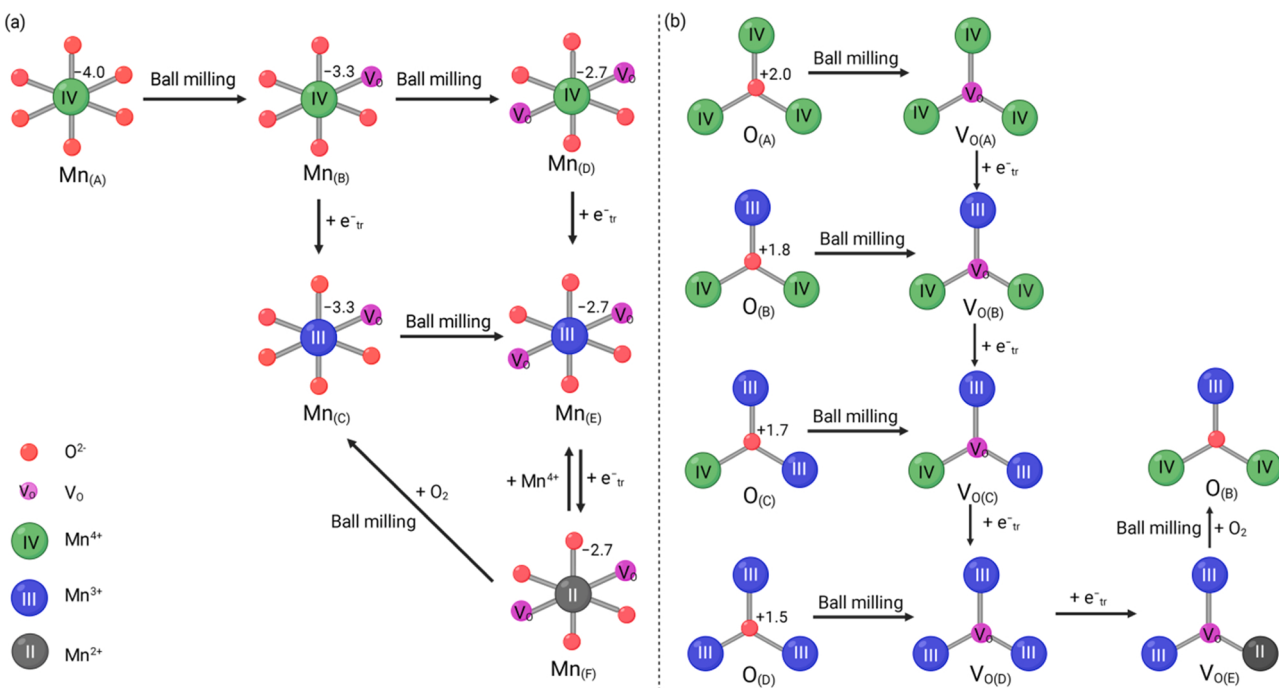
Fig. 5 illustrates the relationship between *k* for the degradation of TBBPA in MnO₂/PMS and Mn ratios or V_O levels on the surface of MnO₂. No clear correlations were observed either between *k* and the Mn⁴⁺ ratio or between *k* and the Mn³⁺ ratio (Fig. 5a and b). As Mn²⁺ ratio increased from 0% to 6.9% and then to 8.5%, *k* increased firstly from 0.0097 to 0.21 min⁻¹ and then decreased to 0.18 min⁻¹ (Fig. 5c). A poor linear correlation was observable between *k* and the Mn²⁺ ratio (*R*² = 0.67). This means that Mn²⁺ is more important than Mn³⁺ and Mn⁴⁺, which is different from previous reports that Mn³⁺ on the surface of MnO₂ increases the activation of PMS [58,59]. As the V_O/O_{SL} ratio increased from 19.4% to 31.6%, *k* increased roughly linearly from 0.0097 to 0.21 min⁻¹, and then decreased to 0.18 min⁻¹ with a further increase in V_O/O_{SL} to 32.6% (Fig. 5d). A better linear relationship was observed between *k* and V_O/O_{SL} (*R*² = 0.85). This suggests a more important role of V_O than Mn²⁺ in the catalytic activity of MnO₂. Bm₂₅-MnO₂ possessed the most abundant V_O and the largest Mn²⁺ ratio, but it exhibited lower activity than bm₂₀-MnO₂, indicating that the catalytic activity of MnO₂ does not merely depend on V_O level. It is noted that there are five types of V_O on the surface of bm_t-MnO₂, among which only one type of V_O associates with Mn²⁺, i.e., (Mn³⁺)₂-V_O-Mn²⁺ (V_{O(E)} in Scheme 1b). Thus, the Mn²⁺ ratio can represent the level of V_{O(E)}, and the subtraction of Mn²⁺ ratio from V_O/O_{SL} ratio would give a value to evaluate the level of V_O associated with Mn³⁺ and/or Mn⁴⁺ (named as V_{O(III+IV)}/O_{SL})

Table 1
Correlations between the Mn species distribution, V_O/O_{SL} ratio and the catalytic activity (in term of the rate constant *k* for the TBBPA degradation) of MnO₂.

Catalyst	<i>t</i> _{bm} /min	Atomic ratio of Mn ⁴⁺ : Mn ³⁺ : Mn ²⁺	V _O /O _{SL} ^a	<i>n</i> _{V_O} , avg ^b	<i>k</i> /min ⁻¹
bm ₀ -MnO ₂	0	45.7: 54.3: 0	0.194	0.81	0.0097
bm ₂ -MnO ₂	2	34.3: 62.2: 3.5	0.263	0.94	0.014
bm ₅ -MnO ₂	5	34.0: 61.6: 4.4	0.269	0.99	0.062
bm ₁₀ -MnO ₂	10	33.5: 61.9: 4.6	0.283	1.04	0.12
bm ₁₅ -MnO ₂	15	34.7: 59.0: 6.3	0.309	1.08	0.19
bm ₂₀ -MnO ₂	20	34.4: 58.7: 6.9	0.316	1.09	0.21
bm ₂₅ -MnO ₂	25	32.9: 58.6: 8.5	0.326	1.15	0.18
bm ₃₀ -MnO ₂	30	34.4: 58.9: 6.7	0.306	1.08	0.13

^a V_O/O_{SL} = O_{c-ads}/O_{SL} was calculated from the devolution of O 1s XPS spectra.

^b The average number of V_O associated with one Mn ion was calculated from the ratio of Mn^{4+/3+/2+} on surface of MnO₂ according to the charge balance theory.



Scheme 1. Schematic diagram for mechanochemically tailoring local chemical environments of Mn (a), and O and V_O (b) on the surface of MnO₂. The numbers near central Mn and O ions represent the calculated charge of central ions gained from their surrounding elements based on the fact that each Mn ion donates 1/6 of charges (i.e., +4/6 charge) to an O²⁻ ion, while each O²⁻ gives 1/3 of charges (i.e., -2/3 charge) to an Mn ion.

including V_{O(A)}, V_{O(B)}, V_{O(C)} and V_{O(D)} in **Scheme 1b**. It is very interesting that there is a good linear correlation between k and V_{O(III + IV)/O_{SL} ($R^2 = 0.95$; **Fig. 5e**). This indicates that V_{O(III + IV)} is much more critical than Mn²⁺-associated one for the activation of PMS, and the redox pair of Mn^{4+/Mn³⁺} is more important than Mn^{3+/Mn²⁺}. The previous studies also show the presence of Mn³⁺ and V_O facilitates the redox reaction of Mn^{4+/Mn³⁺} and the release of oxygen on the surface to enhance the catalytic activity of MnO₂ [50,58,59]. A mechanochemical treatment via ball milling commercial MnO₂ for 20 min produced most abundant V_{O(III + IV)} on the surface of MnO₂, and thus bm₂₀-MnO₂ showed highest activity to activate PMS for the degradation of TBBPA.}

3.5. Origins of the V_O-induced catalysis enhancement

The oxygen vacancy and its adjacent Mn^{3+/Mn⁴⁺} couple are critical for the catalytic activation of PMS on the surface of bm_t-MnO₂. To clarify the role of V_O on the adsorption of PMS and redox reactions of Mn^{x+}, 20 μ L different MnO₂ dispersions (2 g L⁻¹) were coated onto a GCE electrode, dried and then employed for open-circuit potential and CV measurements in Na₂SO₄ solution. As shown in **Fig. 6a**, bare GCE electrode showed an open-circuit potential (φ_{OCP}) of 0.23 V (vs. Ag/AgCl), while MnO₂/GCE electrode caused the value of φ_{OCP} to be more positive (i.e., around 0.36 V). After adding PMS at pH 8, φ_{OCP} of bare GCE and MnO₂/GCE electrodes elevated, and then dropped after further adding TBBPA at pH 8. As controls, the addition of TBBPA at first caused a drop of φ_{OCP} and the further addition of PMS led to an elevation of φ_{OCP} , while the change of φ_{OCP} ($\Delta\varphi_{OCP}$) was negligible after adding the solvent containing diluted H₂SO₄ and/or NaOH solution as pH adjusting agents (**Fig. 6b**). These results suggest that PMS and TBBPA was adsorbed on the surface of electrodes to form oxidative and reductive complexes, respectively. The PMS induced $\Delta\varphi_{OCP}$ was 0.19–0.28 V on MnO₂/GCE electrodes, being larger than that (0.12 V) on bare GCE electrode. This indicates a larger adsorption quantity of PMS on MnO₂/GCE. As t_{bm} was increased from 0 to 30 min, the PMS-induced $\Delta\varphi_{OCP}$ was firstly increased from 0.19 to 0.28 V at t_{bm} = 20 min, and then decreased to 0.25 V at t_{bm} = 30 min. This suggests that a moderate increase of V_O

favors the adsorption of PMS. After further adding TBBPA, the net value of $\Delta\varphi_{OCP}$ compared with that before adding any agents was 0.052–0.18 V, while that on bare GCE was even below zero (i.e., -0.075 V). This suggests that the adsorption of PMS is more favorable than that of TBBPA on MnO₂/GCE, while bare GCE had the opposite result.

Fig. 6c illustrates CV curves of bare GCE and MnO₂/GCE electrodes in deaerated Na₂SO₄ solution. No redox peak was observed on bare GCE electrode, while bm₀-MnO₂/GCE and bm_t-MnO₂/GCE exhibited several redox peaks in the potential range from -0.8 to 1.2 V (vs. Ag/AgCl). Bm₀-MnO₂/GCE showed an oxidation peak at 0.95 V (Ox₁) and two reduction peaks at 0.72 and -0.11 V (Red₁ and Red₂), which was assigned to the oxidation of Mn³⁺ to Mn⁴⁺, the reduction of Mn⁴⁺ to Mn³⁺, and the reduction of Mn³⁺ to Mn²⁺, respectively. Bm_t-MnO₂/GCE showed an additional oxidation peak near 0.5 V (Ox₂) corresponding to the oxidation of Mn²⁺ to Mn³⁺, indicating that Mn²⁺ was generated on the surface of MnO₂ after mechanochemical treatments. Since PMS has a high reduction potential ($E(HSO_5^-/HSO_4^-) = 1.82$ V vs. NHE), both Mn³⁺ and Mn²⁺ can be oxidized by PMS due to the thermodynamic favor. The peak-to-peak potential separation between Ox₁ and Red₁ is 0.2–0.3 V, which is smaller than that (0.5–0.8 V) for the Ox₂/Red₂ pair, suggesting a smaller over-potential for the redox reaction of Mn^{4+/Mn³⁺} than Mn^{3+/Mn²⁺} on the surface of bm_t-MnO₂. Compared with bm₀-MnO₂/GCE, the peak position of Ox₁ on bm_t-MnO₂/GCE moved to higher potential by 10–68 mV as t_{bm} was increased from 5 to 30 min. For the reduction process of Mn⁴⁺ to Mn³⁺, the peak current was 2–3 times smaller than that of Ox₁ on a given bm_t-MnO₂/GCE, and the peak position on bm_t-MnO₂/GCE moved to higher potential by 35–50 mV than that on bm_t-MnO₂/GCE. This implies that the reduction of Mn⁴⁺ to Mn³⁺ is slower than the oxidation of Mn³⁺ to Mn⁴⁺, and it becomes easier on the surface of bm_t-MnO₂ after mechanochemical treatments, due to the excessively positive charge at Mn⁴⁺ in the vicinity of V_O. The peak current for the redox reactions of Mn^{4+/Mn³⁺} on MnO₂/GCE electrodes increased in the order of bm₀-MnO₂ < bm₅-MnO₂ < bm₁₀-MnO₂ < bm₃₀-MnO₂ < bm₂₀-MnO₂, indicating the faster redox reaction of Mn^{4+/Mn³⁺} on the surface of bm₂₀-MnO₂ than those on other MnO₂.

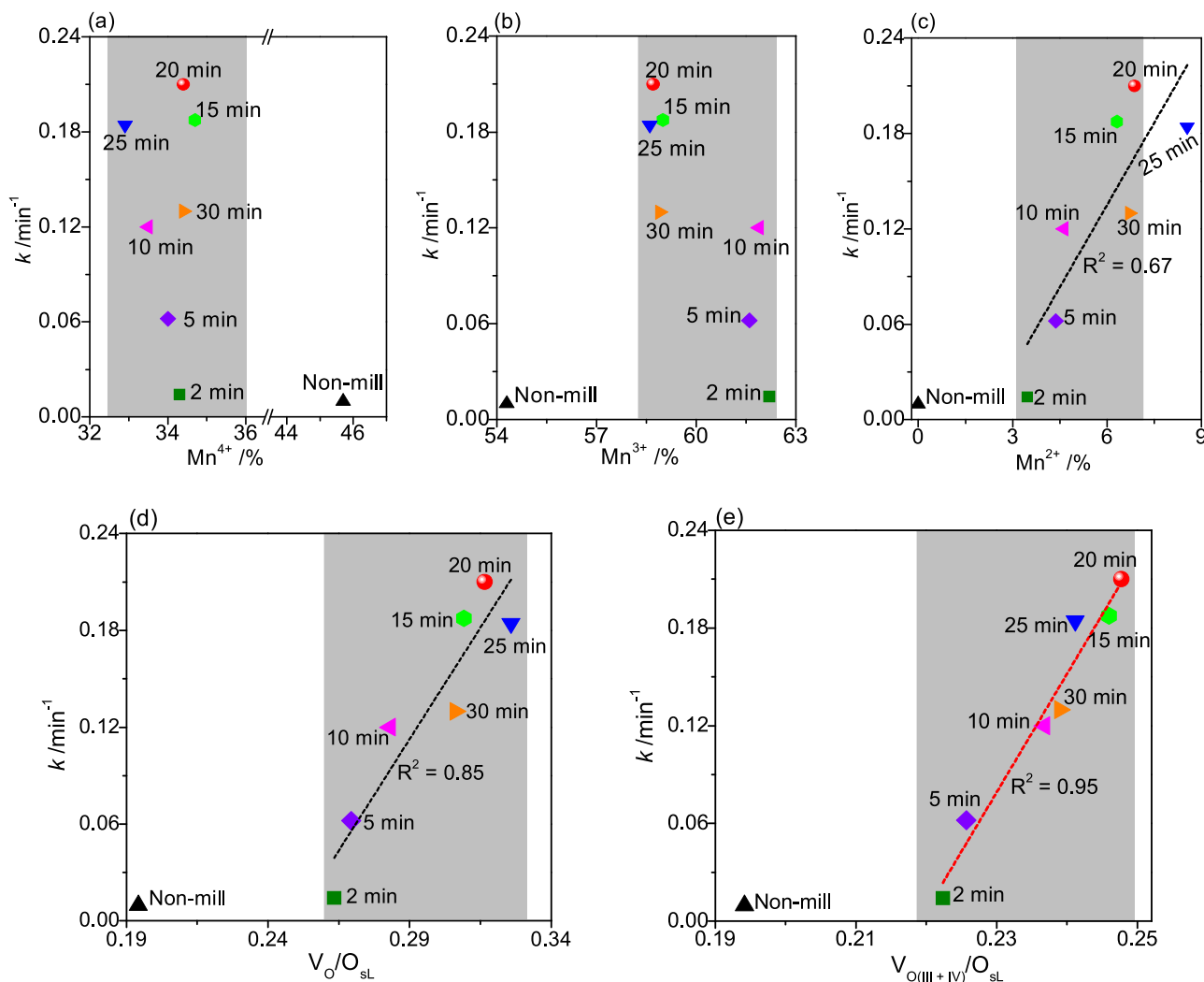


Fig. 5. Relationship between k for the degradation of TBBPA in $\text{bm}_t\text{-MnO}_2/\text{PMS}$ and ratios of Mn^{4+} (a), Mn^{3+} (b), and Mn^{2+} (c), $\text{V}_{\text{O}}/\text{O}_{\text{SL}}$ (d), and $\text{V}_{\text{O(III+IV)}}/\text{O}_{\text{SL}}$ (e) on surface of MnO_2 . $\text{V}_{\text{O(III+IV)}}$ is the adduct of all the V_{O} being associated with Mn^{3+} and Mn^{4+} .

When PMS was added to deaerated Na_2SO_4 solution, each electrode showed similar shape in the CV curve to that in the absence of PMS (Fig. S17). However, the addition of PMS caused a smaller peak current for the redox reaction of $\text{Mn}^{3+}/\text{Mn}^{4+}$, especially for the oxidation of Mn^{3+} to Mn^{4+} (Fig. 6d). This is because that PMS adsorbed on the surface of MnO_2 oxidized Mn^{3+} , which decreased the electron transfer number of Mn^{3+} to the electrode.

$\text{O}_2\text{-TPD}$ measurements were carried out to clarify the role of V_{O} on the mobility of oxygen species in MnO_2 . The sample of $\text{bm}_0\text{-MnO}_2$ showed four stages for the desorption of oxygen species with the peaks located at 340, 470, 530, and 720 °C (Fig. 7), corresponding to the $\text{O}_{\text{c-ads}}$ (such as O_2 , O^- , $\text{O}^{\bullet-}$ and O_2^-), O_{SL} , subsurface O_{L} (O_{SSL}), and bulk O_{L} (O_{bL}), respectively [50]. It is known that V_{O} offers sites for adsorbing and desorbing $\text{O}_{\text{c-ads}}$, and thus $\text{O}_{\text{c-ads}}$ is regarded as an indicator of V_{O} [60]. After ball milling for 5 min, $\text{bm}_5\text{-MnO}_2$ exhibited a new peak at 200 °C assigned to physically-adsorbed oxygen ($\text{O}_{\text{p-ads}}$), while the intensities of three peaks of O_{SL} , O_{SSL} , and O_{bL} decreased to show the formation of more V_{O} . The desorption peak of $\text{O}_{\text{c-ads}}$ in the range of 300–370 °C split into multiply peaks, indicating the distribution change of V_{O} with different local environments. Among five possible types on the surface of $\text{bm}_t\text{-MnO}_2$ (Scheme 1b), $\text{O}_{\text{c-ads}}$ near V_{O} in $\text{Mn}^{4+}\text{-V}_{\text{O}}\text{-}(\text{Mn}^{4+})_2$ ($\text{V}_{\text{O(A)}}$) tends to form the most stable coordination mode between one Mn^{4+} and six O^{2-} , leading to the difficult desorption. In other words, $\text{O}_{\text{c-ads}}$ adsorbed on $\text{V}_{\text{O(A)}}$ is essentially a kind of O_{SL} .

Because of the larger radius and the less positive charge than Mn^{4+} , the presence of Mn^{3+} and/or Mn^{2+} next to V_{O} would make $\text{O}_{\text{c-ads}}$ over there easy to desorb. Based on the comparison with $\text{O}_2\text{-TPD}$ profile of Mn_2O_3 (Fig. S18), $\text{O}_{\text{c-ads}}$ at 300–345 °C may locate on $(\text{Mn}^{3+})_2\text{-V}_{\text{O}}\text{-}(\text{Mn}^{2+})$ ($\text{V}_{\text{O(E)}}$) and $(\text{Mn}^{3+})\text{-V}_{\text{O}}\text{-}(\text{Mn}^{3+})_2$ ($\text{V}_{\text{O(D)}}$), while those at 345–370 °C may locate on $(\text{Mn}^{3+})_2\text{-V}_{\text{O}}\text{-}(\text{Mn}^{4+})$ ($\text{V}_{\text{O(C)}}$) and $\text{Mn}^{3+}\text{-V}_{\text{O}}\text{-}(\text{Mn}^{4+})_2$ ($\text{V}_{\text{O(B)}}$). This indicates that V_{O} exists dominantly in the form of $\text{V}_{\text{O(D)}}$ and $\text{V}_{\text{O(E)}}$ at the initial stage of mechanochemical treatment, probably because that Mn^{4+} in the vicinity of V_{O} prefers to be reduced by e^{-}_{tr} . As t_{bm} was increased to 20 min, the desorption peak of $\text{O}_{\text{c-ads}}$ relating to $\text{V}_{\text{O(D)}}$ and $\text{V}_{\text{O(E)}}$ decreased in intensity, that of O_{SSL} disappeared, and those of $\text{V}_{\text{O(B)}}$ and $\text{V}_{\text{O(C)}}$ and O_{SL} increased, indicating the conversion of O_{SSL} to O_{SL} and then to $\text{V}_{\text{O(B)}}$ and/or $\text{V}_{\text{O(C)}}$ (Scheme 1b). As t_{bm} was further increased to 30 min, $\text{bm}_{30}\text{-MnO}_2$ showed opposite changes in the $\text{O}_2\text{-TPD}$ profile compared with $\text{bm}_{20}\text{-MnO}_2$. The desorption peak of $\text{O}_{\text{c-ads}}$ on $\text{V}_{\text{O(D)}}$ and $\text{V}_{\text{O(E)}}$ near 340 °C increased, while that near 351 °C on $\text{V}_{\text{O(B)}}$ and $\text{V}_{\text{O(C)}}$ decreased. Meanwhile, the desorption peak of O_{SL} decreased, while the peak intensity of O_{SSL} desorption recovered to 70% of the initial value for $\text{bm}_0\text{-MnO}_2$. This means that the mechanochemical treatment for 30 min promotes the conversion of $\text{V}_{\text{O(B, C)}}$ to $\text{V}_{\text{O(D, E)}}$ and O_{SL} through e^{-}_{tr} -involved reduction and oxygenation of V_{O} , respectively, as well as the conversion of O_{SL} to O_{SSL} . Taking into account the results of Figs. 5e, 6 and 7, we may conclude that V_{O} improved the adsorption of PMS on the surface of MnO_2 , and $(\text{Mn}^{3+})_2\text{-V}_{\text{O}}\text{-}(\text{Mn}^{4+})$ and $\text{Mn}^{3+}\text{-V}_{\text{O}}\text{-}(\text{Mn}^{4+})_2$

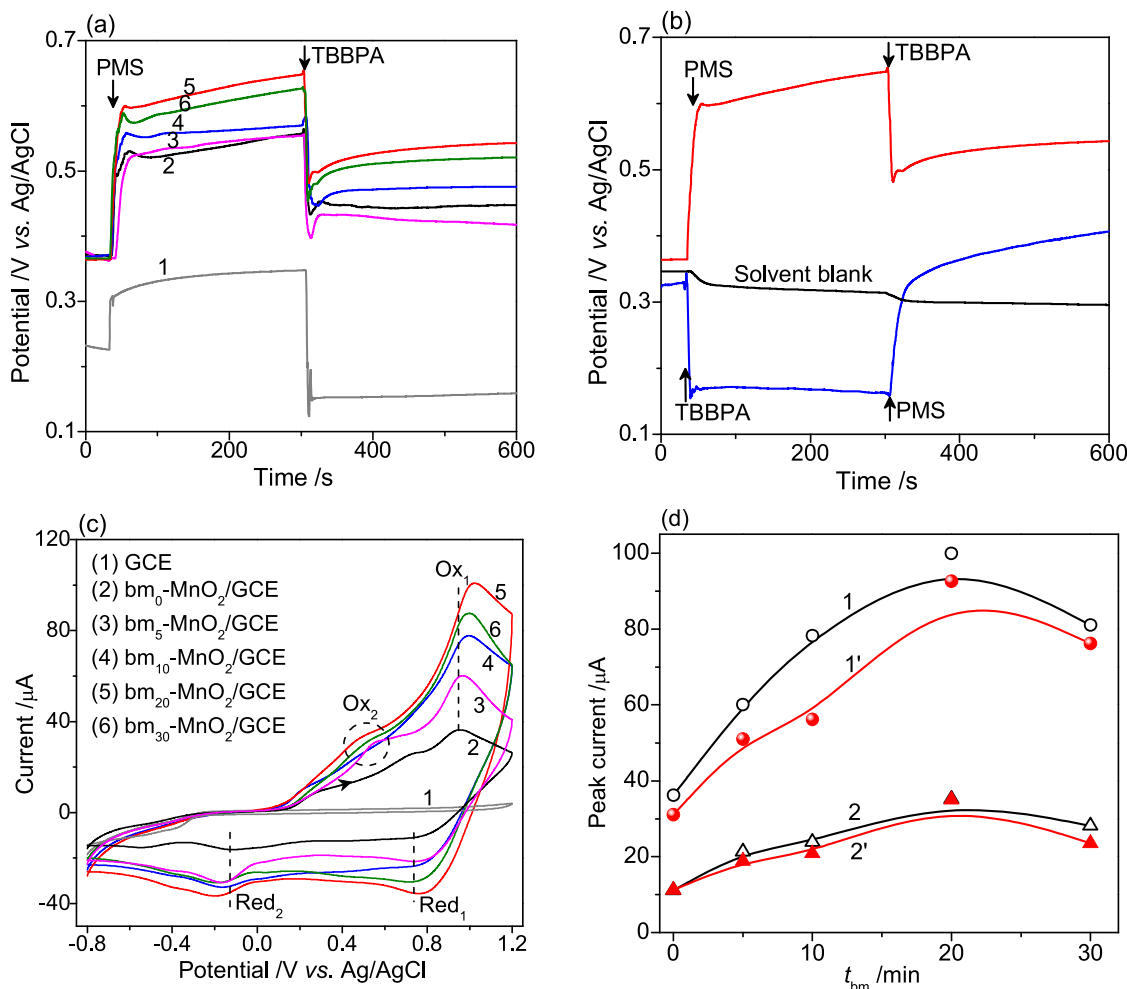


Fig. 6. Open-circuit potential curves of GCE (1) and MnO₂/GCE (2–6) (a), and bm₂₀-MnO₂/GCE (b) in Na₂SO₄ (0.1 mol L⁻¹) before and after adding PMS (0.1 g L⁻¹) or TBBPA (40 mg L⁻¹) at pH 8. Diluted NaOH and H₂SO₄ aqueous solution was used to adjust solution pH to 8, and thus they were chosen as the solvent blank in (b). CV profiles (c) of GCE (1) and MnO₂/GCE (2–6) in deaerated Na₂SO₄ solution. Effect of ball milling time on peak current of Ox₁ (1, 1') and Red₁ (2, 2') for MnO₂/GCE electrodes in the absence (1, 2) and presence (1', 2') of PMS (d).

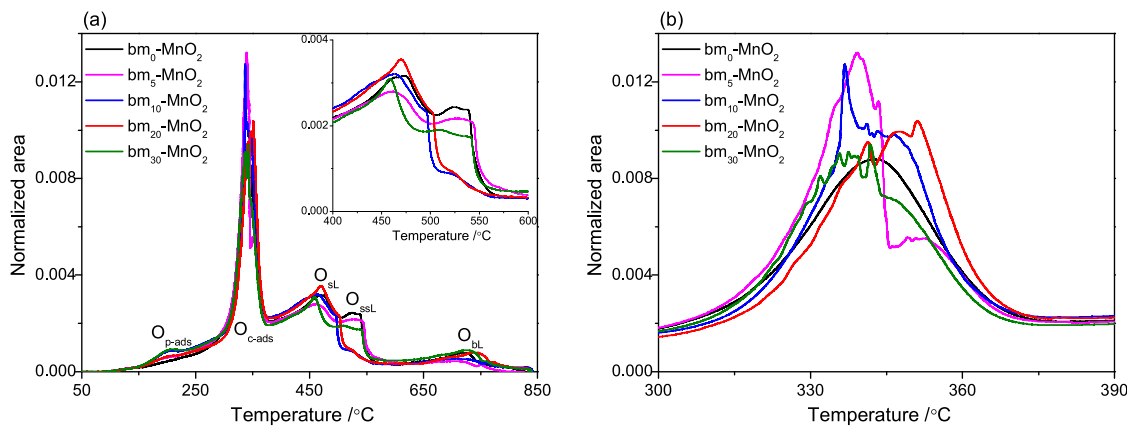


Fig. 7. O₂-TPD profiles (a) and a part of Fig. a in temperature range of 300–390 °C (b) for MnO₂ before (bm₀-MnO₂) and after different ball milling time (bm_t-MnO₂).

play critical roles in the catalytic activation of PMS by MnO₂.

3.6. Insight into reaction mechanism

To explore reaction mechanism in bm₂₀-MnO₂/PMS for the TBBPA degradation, the generation of ROSs was identified by EPR

measurements using DMPO and TEMP as spin-trapping agents and quenching experiments using ethanol, t-butyl alcohol and β-carotene as quenchers. The results confirmed that ¹O₂ was the dominant ROS for the degradation of TBBPA, and the generation of ¹O₂ increased with an order of PMS < bm₀-MnO₂/PMS < bm₂₀-MnO₂/PMS (Fig. S19). Such proposal is further proved by the facts that no degradation of

parachlorobenzoic acid was observed in $\text{bm}_{20}\text{-MnO}_2/\text{PMS}$, while almost complete degradation was achieved in $\text{Co}^{2+}/\text{PMS}$ as a typical $\text{SO}_4^{\bullet-}$ -mediated oxidation system (Fig. S20). This is because parachlorobenzoic acid can react quickly with both $\bullet\text{OH}$ and $\text{SO}_4^{\bullet-}$ (5.2×10^9 and $3.6 \times 10^8 \text{ M}^{-1} \text{ s}^{-1}$, respectively) [61], but not $^1\text{O}_2$.

The generation of $^1\text{O}_2$ may come from three possible pathways: (1) the self-decomposition of PMS [26]; (2) the reaction of PMS with $\text{O}_2^{\bullet-}$ which is formed from single-electron reduction of dissolved O_2 in solution [60]; (3) the reaction of PMS with the released lattice oxygen of MnO_2 [62,63]. When N_2 was purged to remove dissolved O_2 or chloroform as a quencher of $\text{O}_2^{\bullet-}$ was added, the degradation of TBBPA in $\text{bm}_{20}\text{-MnO}_2/\text{PMS}$ did not change (Fig. S21), excluding the role of dissolved O_2 and $\text{O}_2^{\bullet-}$.

If the surface lattice oxygen (O_{SL}) of MnO_2 participates in the generation of $^1\text{O}_2$, the consumption and regeneration of O_{SL} would influence its catalytic activity. The reusability of $\text{bm}_{20}\text{-MnO}_2$ was checked for the 5 successive degradation cycles of TBBPA in the presence of PMS under air and N_2 atmosphere. It was found the purged N_2 did not influence the degradation of TBBPA in each cycle (Figs. 8a and S22), further confirming no effect of dissolved O_2 . The degradation rate of TBBPA was slightly decreased in the last two runs, but all the added TBBPA was nearly removed as the reaction time was increased to 30 min (Fig. 8b). This suggests that $\text{bm}_{20}\text{-MnO}_2$ could be reused with high catalytic activity. The leached Mn ions in each degradation solution were below the detection limit (i.e., 0.010 mg L^{-1}) of ICP-AES, and the leached solution

from $\text{bm}_{20}\text{-MnO}_2$ had no effect on the degradation of TBBPA in the presence of PMS (Fig. S23). This indicated that the degradation of TBBPA is attributed to the heterogeneous reaction over the surface of MnO_2 . No obvious changes were detected in XRD patterns and high-resolution XPS spectra of Mn 2p after five cycles (Figs. S24, S25a and b). This indicated that the degradation of TBBPA is attributed to heterogeneous reactions on the surface of MnO_2 , and the crystalline structure of $\gamma\text{-MnO}_2$ was not changed. However, the atomic percentage of O_{SL} decreased by ca. 19%, and that of $\text{O}_{\text{c-ads}}$ and physically adsorbed water ($\text{H}_2\text{O}_{\text{ads}}$) increased by ca. 9% and 10% after 5 cycles, respectively (Figs. 8c, S25c and d). This suggests the loss of O_{SL} and the generation of $\text{O}_{\text{c-ads}}$ and $\text{H}_2\text{O}_{\text{ads}}$ on the surface of MnO_2 during degradation reactions. In $\text{bm}_{20}\text{-MnO}_2/\text{PMS}$ (50 mL), the self-decomposition of 0.1 g L^{-1} PMS ($8.13 \mu\text{mol}$) in each run would generate $4.07 \mu\text{mol} ^1\text{O}_2$, which is lower than the theoretical demand of $^1\text{O}_2$ ($23.7 \mu\text{mol}$), calculated from Eq. (1) for the TOC removal of 43%. This indicates that in addition to PMS, lattice oxygen on the surface of MnO_2 is also the source of $^1\text{O}_2$. The total O in 0.3 g L^{-1} MnO_2 is $345.1 \mu\text{mol}$, and the consumed O_{SL} would generate the maximum possible amount of $65.6 \mu\text{mol} ^1\text{O}_2$. The total amount of $^1\text{O}_2$ generated from both PMS and MnO_2 would be $86.0 \mu\text{mol}$, still being less than the $^1\text{O}_2$ demand in five runs ($118.5 \mu\text{mol}$). These results indicate O_{SL} of MnO_2 must be regenerated, and the water solvent may be involved in the regeneration of O_{SL} .

To clarify the role of water solvent, 30 mg $\text{bm}_{20}\text{-MnO}_2$ was dispersed in 0.1 mL H_2^{18}O and kept overnight to allow V_O and $^{16}\text{O}_{\text{SL}}$ being filled or

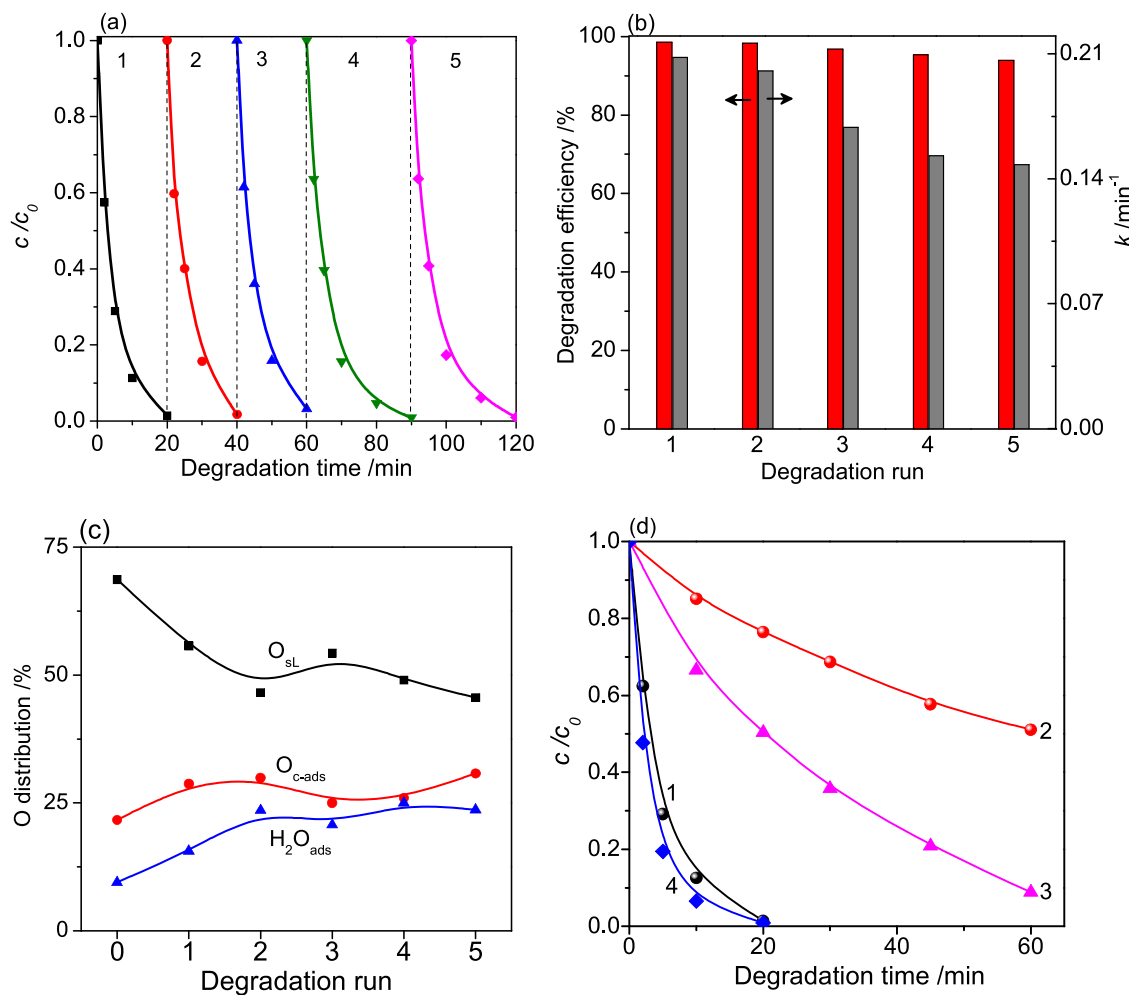
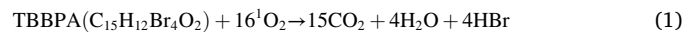


Fig. 8. Successive degradation cycles of TBBPA (a), and its degradation efficiency in 20 min and pseudo-first-order degradation rate constant (k) (b) over $\text{bm}_{20}\text{-MnO}_2$ in the presence of PMS under N_2 . The dot lines in (a) indicate that the start of a new cycle of degradation after dispersing recovered catalysts into fresh TBBPA and PMS solution. Distribution of O element calculated from O 1s XPS spectra (c) on the surface of $\text{bm}_{20}\text{-MnO}_2$ before and after successive degradation cycles. Degradation of TBBPA (d) in the presence of PMS and $\text{bm}_{20}\text{-MnO}_2$ before (1) and after a pre-treatment with PMS/ H_2^{18}O (2), H_2^{18}O (3) and PMS/ H_2O (4).

exchanged with ^{18}O of H_2^{18}O . The collected samples were washed with general distilled water to remove the residual H_2^{18}O , followed by vacuum drying. When the $^{18}\text{O}_{\text{SL}}$ -labeled $\text{bm}_{20}\text{-MnO}_2$ was used to degrade TBBPA in the presence of PMS, the TBBPA degradation was significantly suppressed and k decreased from 0.21 to 0.039 min^{-1} with a $^{16}\text{O}/^{18}\text{O}$ overall kinetic isotope effect (KIE) of 5.38 (Fig. 8d). This is similar to the previous report that the oxidation of organic pollutants by ^{18}O -labeled ROS such as $\bullet^{18}\text{OH}$ radicals was significantly decreased [33], due to the heavy atom isotope effects. It indicates that $^{18}\text{O}_{\text{SL}}$ of MnO_2 can react with PMS to generate ^{18}O -labeled $^{1}\text{O}_2$. When 30 mg $\text{bm}_{20}\text{-MnO}_2$ was pre-treated by 0.1 mL H_2^{18}O containing 10 mg PMS, the obtained $\text{bm}_{20}\text{-MnO}_2$ led to the decreased k to 0.011 min^{-1} with a larger $^{16}\text{O}/^{18}\text{O}$ KIE of 19.1 than that for pre-treated $\text{bm}_{20}\text{-MnO}_2$ with H_2^{18}O alone (Fig. 8d). As a control, almost no change of k was observed for the pre-treated MnO_2 with PMS/ H_2O (Fig. 8d). In the pre-treatment, the reaction of MnO_2 with PMS promoted the consumption of $^{16}\text{O}_{\text{SL}}$, leading to the regeneration of more $^{18}\text{O}_{\text{SL}}$ thereby decreasing the formation of $^{1}\text{O}_2$ and consequently decreasing the degradation of TBBPA. Moreover, the calculated values of $^{16}\text{O}/^{18}\text{O}$ KIE are much larger than those (1.01–1.04) for the ^{18}O associated O_2 evolution with $\text{O}-\text{O}$ bond formation being the rate-determining step [64]. This suggests that the $^{1}\text{O}_2$ -mediated oxidation of TBBPA in MnO_2/PMS involved multiply ^{18}O

associated bond formation and breakage pathways such as the breakage of $\text{Mn}-\text{O}$ bond, the reaction of in-situ released O_{SL} with PMS, the formation of $\text{O}-\text{O}$ bond in $^{1}\text{O}_2$, and the addition of $^{1}\text{O}_2$ to TBBPA and the degradation products.



Raman spectra were used to explore the activation reaction of PMS on the surface of $\text{bm}_0\text{-MnO}_2$ and $\text{bm}_{20}\text{-MnO}_2$. As shown in Fig. 9a, PMS powders showed characteristic Raman bands of HSO_5^- centered at 1059, 890, 750, 423 and 258 cm^{-1} arising from the stretching vibration of $\text{S=O}(\nu_{\text{S=O}})$, $\text{O-O}(\nu_{\text{O-O}})$ and $\text{S-O}(\nu_{\text{S-O}})$, and the rocking mode of SO_3 (δ_{SO_3}) and the bending vibration of S-O-O ($\beta_{\text{S-O-O}}$), respectively [65]. Since KHSO_4 is present in potassium oxone, it was also observed Raman bands arising from S=O at 1036 and 1007 cm^{-1} and $\nu_{\text{S-OH}}$ near 890 (overlapping with the $\nu_{\text{O-O}}$ band of HSO_5^-) and 865 cm^{-1} in chain and dimer HSO_4^- together with δ_{SO_3} near 423 cm^{-1} (overlapping with the δ_{SO_3} band of HSO_5^-), respectively [66,67]. When Raman spectra was normalized to the $\nu_{\text{S=O}}$ peak intensity of HSO_5^- at 1059 cm^{-1} , the relative intensity of peaks at 890, 750, 423 and 258 cm^{-1} (I'_{890} , I'_{750} , I'_{423} and I'_{258}) was 0.89, 0.37, 0.18 and 0.098, respectively. After mixing PMS with $\text{bm}_0\text{-MnO}_2$ or $\text{bm}_{20}\text{-MnO}_2/\text{PMS}$, the bands of HSO_4^- at 1036, 1007 cm^{-1} and 865 cm^{-1} disappeared, and a new peak appeared at

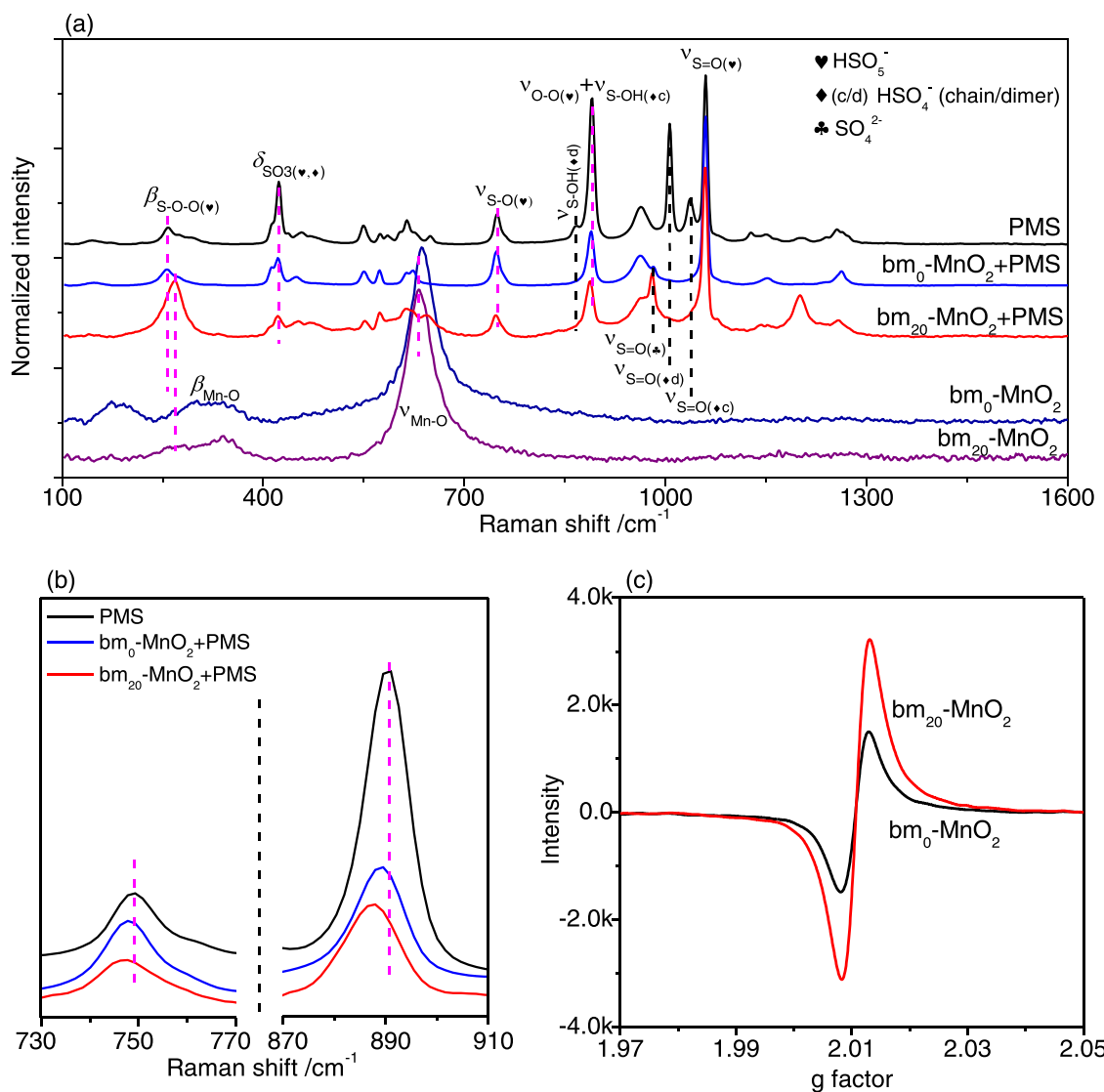


Fig. 9. Raman spectra (a) and a part of Fig. a in Raman shift of 730–770 and 870–910 cm^{-1} (b) for solid PMS, MnO_2 and their mixture at a mass ratio of 1: 2. EPR spectra (c) of solid $\text{bm}_0\text{-MnO}_2$ and $\text{bm}_{20}\text{-MnO}_2$ powders.

980 cm⁻¹ corresponding to ν_{S-O} of SO₄²⁻ [68], indicating the dissociation of HSO₄⁻ to SO₄²⁻ on the surface of MnO₂ before and after mechanochemical treatment. For bm₀-MnO₂/PMS, I'_{890} and I'_{423} of PMS relating to ν_{O-O} (HSO₅⁻) + ν_{S-OH} (HSO₄⁻) and δ_{SO_3} (HSO₅⁻ and HSO₄⁻) decreased to 0.30 and 0.16, respectively, whereas I'_{750} and I'_{258} relating to ν_{S-O} and β_{S-O-O} of HSO₅⁻ was nearly unchanged. This suggests that the decreased I'_{890} and I'_{423} were only contributed to the conversion of HSO₄⁻ to SO₄²⁻, and that the interfacial interaction between bm₀-MnO₂ and HSO₅⁻ was negligible. Comparably, bm₂₀-MnO₂/PMS showed a blue shift for the ν_{O-O} and ν_{S-O} bands of HSO₅⁻ with lower intensities ($I'_{890} = 0.27$, $I'_{750} = 0.12$), a larger intensity change of δ_{SO_3} in HSO₅⁻ and HSO₄⁻ and ν_{S-O} of SO₄²⁻ ($I'_{423} = 0.12$, $I'_{980} = 0.37$) (Fig. 9a and b). This indicates that the adsorption of HSO₅⁻ on the surface of bm₂₀-MnO₂ not only weakened the peroxide bond and the S—O bond, but also improved the decomposition to SO₄²⁻. Meanwhile, two new Raman peaks appeared at 268 and 1201 cm⁻¹, and the former one is attributed to β_{Mn-O} . This indicates the generation of O_{c-ads} on bm₂₀-MnO₂. In addition, the band of ν_{Mn-O} in bm₂₀-MnO₂ became broader after mixing with PMS, signifying a more disordered structure of [MnO₆] octahedral. After HSO₅⁻ was adsorbed on the surface of MnO₂, both Mn³⁺ and e^{-tr} may induce the reductive decomposition of PMS. In order to explore the concentration change of e^{-tr} in MnO₂, solid EPR measurements were conducted. As shown in Fig. 9c, bm₀-MnO₂ showed a characteristic and symmetrical peak with at g = 2.010 originated from the unpaired electrons at V_O sites [40], while the EPR intensity of e^{-tr} in bm₂₀-MnO₂ increased by 1.2 times. This indicates that as-received γ -MnO₂ contains a certain amount of V_O, and a mechanochemical treatment creates more V_O and e^{-tr}.

DFT calculations have been conducted to calculate the role of V_O on the catalytic activity of MnO₂. γ -MnO₂ before and after mechanochemical treatments showed three low-index facets (i.e., (120), (131) and (300)), among which (120) facet possessed lower surface energy (0.045 eV Å⁻²) than (131) and (300) facets (0.059 and 0.149 eV Å⁻², respectively). Then, the adsorption energies of PMS ($E_{ads, PMS}$) on the planes of perfect and V_O-defective (120) facet were calculated by DFT and the final stable configurations were illustrated in Fig. 10. Perfect (120) facet bonded two O²⁻ of SO₃ group in HSO₅⁻ on two different Mn^{x+} with the positive $E_{ads, PMS}$ of 0.247 eV (Fig. 10a), suggesting an endothermic and unstable adsorption process. In addition,

intramolecular hydrogen bond was observed in H—O—O group of HSO₅⁻. For V_O-defective (120) facet, the adsorption of PMS showed different configuration with the negative $E_{ads, PMS}$ of -2.704 eV (Fig. 10b), indicating a stable and exothermic chemical process. The one O⁻ of peroxy group in HSO₅⁻ were firstly trapped by V_O to interact with V_O-associated Mn^{x+} and two O²⁻ of SO₃ group in HSO₅⁻ were bonded with another two Mn^{x+} ions. The strong charge transfer from V_O-associated Mn^{x+} to PMS and the intramolecular hydrogen transfer enabled the heterolysis of peroxy bond to form surface bound O^{•-} (O^{•-}_{ads}) and HSO₄⁻ (HSO₄⁻_{ads}). This agrees with Raman results.

Based on the above results and discussion, Scheme 2 illustrates the reaction mechanism of V_O-rich bm₀-MnO₂ to activate PMS for the generation of 1O_2 . PMS (HSO₅⁻) preferentially adsorbs on V_O sites of bm₀-MnO₂, owing to the strong affinity of V_O for peroxy-bonds [69]. Mn³⁺ in the vicinity of V_O reduces PMS to generate Mn⁴⁺, SO₄²⁻, H⁺, and O^{•-} adsorbed on V_O (O^{•-}_{ads}), and O_{ads}^{•-} is then oxidized by V_O-associated Mn⁴⁺ to generate oxygen atom (O[•]). On the other hand, O_{SL} in vicinity of Mn³⁺ on the surface of bm₀-MnO₂ is released to generate O^{•ads}, V_O and e^{-tr} [63]. The adsorbed PMS reacts with O^{•ads} to generate 1O_2 [62]. The reduction of Mn⁴⁺ consumes e^{-tr} to improve the regeneration of O^{•ads}. In addition, e^{-tr} may reduce PMS to generate SO₄²⁻, H⁺, and O^{•-}_{ads}, of which O^{•-}_{ads} would finally convert to 1O_2 . After O_{SL} was consumed, water can be adsorbed on V_O to allow the regeneration of O_{SL} on the surface of MnO₂. When V_O is surrounded by the three Mn⁴⁺ ions, the oxidation of Mn⁴⁺ by PMS is thermodynamic unfavorable, while its reduction by PMS is slow to produce SO₅^{•-} with low activity [15]. In addition, O_{c-ads} on Mn⁴⁺-V_O-(Mn⁴⁺)₂ desorbed more difficult than those on other types of V_O (Fig. 7). Since bm₀-MnO₂ possessed a greater amount of Mn⁴⁺-V_O-(Mn⁴⁺)₂ than bm₁-MnO₂, it showed lower catalytic activity than bm₁-MnO₂. When V_O is associated with Mn²⁺, it would indeed allow the electron transfer from Mn²⁺ to adsorbed PMS, but the consequent reduction of Mn³⁺ needs to overcome the higher thermodynamic energy barrier than the reduction of Mn⁴⁺ (Fig. 6c). Moreover, such V_O allowed the removal of O_{c-ads} at lower temperature than those near both Mn⁴⁺ and Mn³⁺ (Fig. 7), suggesting the lower affinity of Mn²⁺-associated V_O for adsorbing oxygen-containing species than V_O near both Mn⁴⁺ and Mn³⁺ [70]. Thus, a good MnO₂ catalyst must achieve a fast redox reaction of Mn^{x+}/Mn^{(x+)-} and a balance between the adsorption and desorption of ROSs. All these three requirements are not merely dependent on the level of V_O, but also influenced by the local chemical environment of V_O, i.e., the valence state of its neighboring metastable cations. Compared with the pair of Mn³⁺/Mn²⁺, the redox reaction of Mn⁴⁺/Mn³⁺ has a smaller over-potential on the surface of MnO₂ (Fig. 6c). Among five types V_O, both Mn³⁺- and Mn⁴⁺-associated V_O possessed moderate affinity for adsorbing and desorbing O_{c-ads} (Fig. 7). The presence of V_O near Mn⁴⁺ and Mn³⁺ not only improves the redox cycle of Mn³⁺/Mn⁴⁺, but also promotes the release of O_{SL}, thus enhancing the activity of bm-MnO₂ to activate PMS for the generation of 1O_2 and the consequent TBBPA degradation.

4. Conclusion

A mechanochemical method was developed via ball milling commercial MnO₂ for preparing V_O-rich MnO₂ as a catalyst towards the PMS activation for the degradation of TBBPA. It was observed that the V_O-rich MnO₂ obtained by ball milling commercial MnO₂ at 350 rpm for 20 min (bm₂₀-MnO₂) exhibited the best catalytic activity, which increased the degradation rate constant of TBBPA by 22 times in comparison with that with un-milled MnO₂ as the catalyst. The use of bm₂₀-MnO₂ catalytically activated PMS to produce 1O_2 as the dominant ROS for the degradation of TBBPA. ¹⁸O-labeling tests confirmed that both PMS and lattice oxygen of MnO₂ were the source of 1O_2 , and the O of water solvent participated in the regeneration of lattice oxygen on/in MnO₂. It was revealed that the catalytic activity of MnO₂ was influenced by the level of V_O and its local environment (i.e., the oxidation state of V_O-associated Mn ions). Both the redox reactions of Mn⁴⁺/Mn³⁺ and the

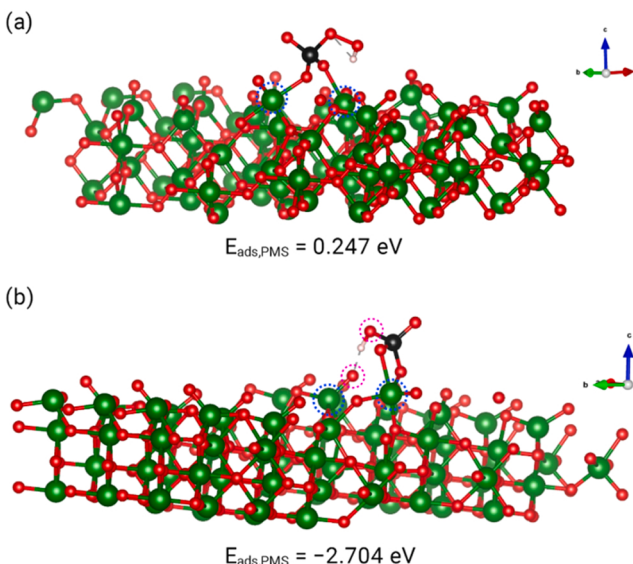
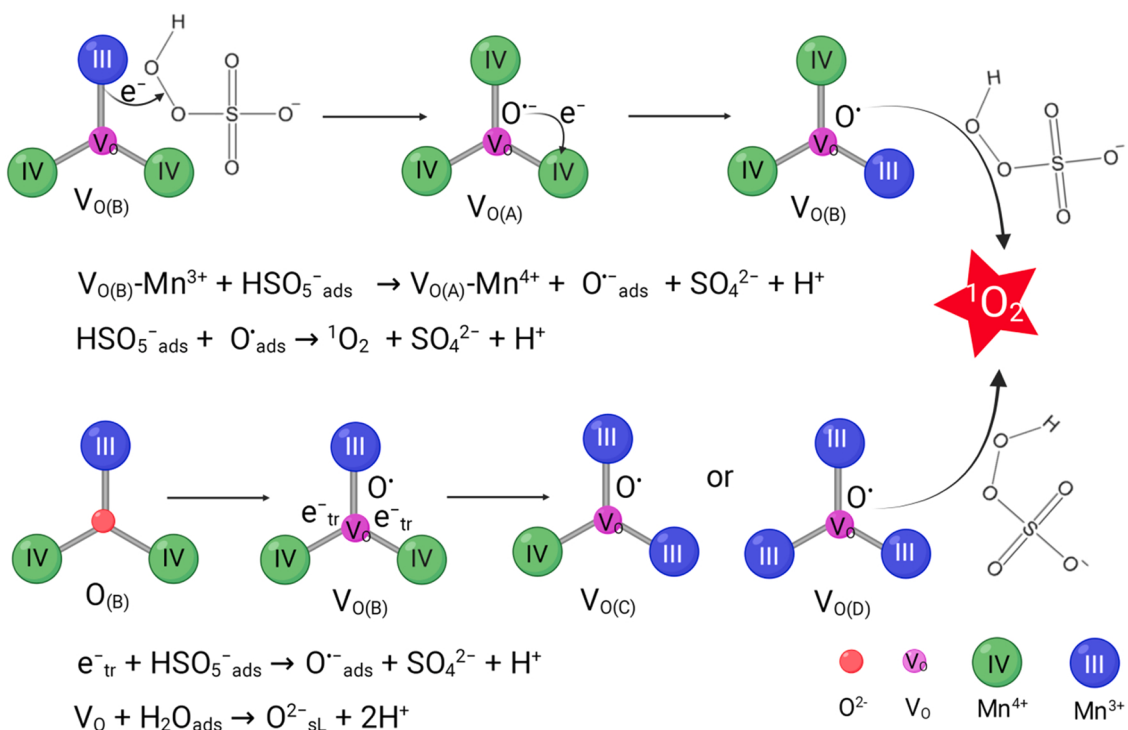


Fig. 10. Adsorption configuration and energy of PMS (HSO₅⁻) on perfect (a) and V_O-defective (b) (120) facet of γ -MnO₂. Mn, O, S and H atoms are green, red, black and white spheres, respectively. Red open circles represent the O in peroxy group of PMS, while blue open circles represent Mn ions that interact with PMS.



Scheme 2. Schematic diagram for the activation of PMS by the redox reaction of $\text{Mn}^{4+}/\text{Mn}^{3+}$ and the released oxygen ions on the surface of V_0 -rich MnO_2 .

released lattice oxygen on the surface of V_0 -rich MnO_2 contributed to the PMS activation for the generation of ${}^1\text{O}_2$. V_0 not only enhanced the redox cycling of $\text{Mn}^{3+}/\text{Mn}^{4+}$, but also promoted the mobility and exchange of oxygen, thus accelerating the activation of PMS. This work provides an alternative method to tailor V_0 levels on the surface of metal oxides for enhancing their catalytic activity.

CRediT authorship contribution statement

Sylvestre Ndayiragije: Methodology, Validation, Writing – original draft. **Yifan Zhang:** Validation, Investigation. **Yuqi Zhou:** Validation. **Zhou Song:** Investigation. **Nan Wang:** Conceptualization, Methodology, Writing – review & editing. **Tetsuro Majima:** Writing – review & editing. **Lihua Zhu:** Supervision, Writing – review & editing.

Declaration of Competing Interest

The authors declare that they have no known competing financial interests or personal relationships that could have appeared to influence the work reported in this paper.

Acknowledgments

The authors acknowledge the funding support from the National Natural Science Foundation of China (Nos. 21976063 and 22076052). We also thank the Innovation and Talent Recruitment Base of New Energy Chemistry and Device (B21003) as well as the Analytical and Testing Center of Huazhong University of Science and Technology and Hubei Province Geological Experimental Testing Center for providing facilities to conduct characterizations of catalysts. The graphic abstract were created with [BioRender.com](#) under an academic lab subscription.

Appendix A. Supplementary material

Supplementary data associated with this article can be found in the online version at [doi:10.1016/j.apcatb.2022.121168](https://doi.org/10.1016/j.apcatb.2022.121168).

References

- [1] Y. Ding, L. Zhu, N. Wang, H. Tang, Sulfate radicals induced degradation of tetrabromobisphenol A with nanoscaled magnetic CuFe_2O_4 as a heterogeneous catalyst of peroxymonosulfate, *Appl. Catal. B* 129 (2013) 153–162.
- [2] W.-D. Oh, Z. Dong, T.-T. Lim, Generation of sulfate radical through heterogeneous catalysis for organic contaminants removal: current development, challenges and prospects, *Appl. Catal. B* 194 (2016) 169–201.
- [3] Z. Xu, Y. Wu, Q. Ji, T. Li, C. Xu, C. Qi, H. He, S. Yang, S. Li, S. Yan, C. Sun, L. Zhang, Z. Zou, Understanding spatial effects of tetrahedral and octahedral cobalt cations on peroxymonosulfate activation for efficient pollution degradation, *Appl. Catal. B* 291 (2021), 120072.
- [4] S. Li, J. Huang, Z.-F. Ye, Y. Wang, X. Li, J. Wang, L. Li, The mechanism of metal- H_2O_2 complex immobilized on MCM-48 and enhanced electron transfer for effective perozone ozonation of sulfamethazine, *Appl. Catal. B* 280 (2021), 119453.
- [5] W. Chen, J. Xie, X. Li, L. Li, Oxygen vacancies and lewis sites activating $\text{O}_3/\text{H}_2\text{O}_2$ at wide pH range via surface electron transfer over $\text{CeO}_x@\text{SiO}_2$ for nitrobenzene mineralization, *J. Hazard. Mater.* 406 (2020), 124766.
- [6] J. Wang, S. Wang, Activation of persulfate (PS) and peroxymonosulfate (PMS) and application for the degradation of emerging contaminants, *Chem. Eng. J.* 334 (2018) 1502–1517.
- [7] M.M. Mian, G. Liu, B. Fu, Y. Song, Facile synthesis of sludge-derived $\text{MnO}_{x-\text{N}}$ -biochar as an efficient catalyst for peroxymonosulfate activation, *Appl. Catal. B* 255 (2019), 117765.
- [8] F. Ghanbari, M. Moradi, Application of peroxymonosulfate and its activation methods for degradation of environmental organic pollutants: review, *Chem. Eng. J.* 310 (2017) 41–62.
- [9] M. Chen, L. Zhu, S. Liu, R. Li, N. Wang, H. Tang, Efficient degradation of organic pollutants by low-level Co^{2+} catalyzed homogeneous activation of peroxymonosulfate, *J. Hazard. Mater.* 371 (2019) 456–462.
- [10] H. Ma, Y. Zhang, L. Zhu, T. Majima, N. Wang, Efficient activation of peroxymonosulfate on cobalt hydroxylchloride nanoplates through hydrogen bond for degradation of tetrabromobisphenol A, *Chem. Eng. J.* 413 (2021), 127480.
- [11] P. Hu, M. Long, Cobalt-catalyzed sulfate radical-based advanced oxidation: a review on heterogeneous catalysts and applications, *Appl. Catal. B* 181 (2016) 103–117.
- [12] D. Jampaiah, V.K. Velisoju, P. Venkataswamy, V.E. Coyle, A. Nafady, B.M. Reddy, S.K. Bhargava, Nanowire morphology of mono- and bidoped $\alpha\text{-MnO}_2$ catalysts for remarkable enhancement in soot oxidation, *ACS Appl. Mater. Interfaces* 9 (2017) 32652–32666.
- [13] T. Pan, H. Deng, S. Kang, Y. Zhang, W. Lian, C. Zhang, H. He, Facile homogeneous precipitation method to prepare MnO_2 with high performance in catalytic oxidation of ethyl acetate, *Chem. Eng. J.* 417 (2021), 129246.
- [14] E. Saputra, S. Muhammad, H. Sun, H.M. Ang, M.O. Tadé, S. Wang, Different crystallographic one-dimensional MnO_2 nanomaterials and their superior performance in catalytic phenol degradation, *Environ. Sci. Technol.* 47 (2013) 5882–5887.

- [15] E. Saputra, S. Muhammad, H. Sun, H.-M. Ang, M.O. Tadé, S. Wang, Manganese oxides at different oxidation states for heterogeneous activation of peroxyomonosulfate for phenol degradation in aqueous solutions, *Appl. Catal. B* 142–143 (2013) 729–735.
- [16] E. Saputra, S. Muhammad, H. Sun, H.-M. Ang, M.O. Tadé, S. Wang, Shape-controlled activation of peroxyomonosulfate by single crystal α -Mn₂O₃ for catalytic phenol degradation in aqueous solution, *Appl. Catal. B* 154–155 (2014) 246–251.
- [17] Y. Yang, P. Zhang, K. Hu, X. Duan, Y. Ren, H. Sun, S. Wang, Sustainable redox processes induced by peroxyomonosulfate and metal doping on amorphous manganese dioxide for nonradical degradation of water contaminants, *Appl. Catal. B* 286 (2021), 119903.
- [18] S. Luo, L. Duan, B. Sun, M. Wei, X. Li, A. Xu, Manganese oxide octahedral molecular sieve (OMS-2) as an effective catalyst for degradation of organic dyes in aqueous solutions in the presence of peroxyomonosulfate, *Appl. Catal. B* 164 (2015) 92–99.
- [19] N. Tian, X. Tian, Y. Nie, C. Yang, Z. Zhou, Y. Li, Biogenic manganese oxide: an efficient peroxyomonosulfate activation catalyst for tetracycline and phenol degradation in water, *Chem. Eng. J.* 352 (2018) 469–476.
- [20] W. Tang, X. Wu, D. Li, Z. Wang, G. Liu, H. Liu, Y. Chen, Oxalate route for promoting activity of manganese oxide catalysts in total VOCs' oxidation: effect of calcination temperature and preparation method, *J. Mater. Chem. A* 2 (2014) 2544–2554.
- [21] S.C. Kim, W.G. Shim, Catalytic combustion of VOCs over a series of manganese oxide catalysts, *Appl. Catal. B* 98 (2010) 180–185.
- [22] H. Chai, Z. Zhang, Y. Zhou, L. Zhu, H. Lv, N. Wang, Roles of intrinsic Mn³⁺ sites and lattice oxygen in mechanochemical de bromination and mineralization of decabromodiphenyl ether with manganese dioxide, *Chemosphere* 207 (2018) 41–49.
- [23] M. Sun, L. Yu, F. Ye, G. Diao, Q. Yu, Z. Hao, Y. Zheng, L. Yuan, Transition metal doped cryptomelane-type manganese oxide for low-temperature catalytic combustion of dimethyl ether, *Chem. Eng. J.* 220 (2013) 320–327.
- [24] N. Jabeen, Q. Xia, S.V. Savilov, S.M. Aldoshin, Y. Yu, H. Xia, Enhanced pseudocapacitive performance of α -MnO₂ by cation preinsertion, *ACS Appl. Mater. Interfaces* 8 (2016) 33732–33740.
- [25] T. Uematsu, Y. Miyamoto, Y. Ogasawara, K. Suzuki, K. Yamaguchi, N. Mizuno, Molybdenum-doped α -MnO₂ as an efficient reusable heterogeneous catalyst for aerobic sulfide oxygenation, *Catal. Sci. Technol.* 6 (2016) 222–233.
- [26] Y. Zhao, H. An, G. Dong, J. Feng, T. Wei, Y. Ren, J. Ma, Oxygen vacancies induced heterogeneous catalysis of peroxyomonosulfate by Ni-doped AgFeO₂ materials: evolution of reactive oxygen species and mechanism, *Chem. Eng. J.* 388 (2020), 124371.
- [27] S.L. James, C.J. Adams, C. Bolm, D. Braga, P. Collier, T. Frisić, F. Grepioni, K. D. Harris, G. Hyett, W. Jones, A. Krebs, J. Mack, L. Maini, A.G. Orpen, I.P. Parkin, W.C. Shearouse, J.W. Steed, D.C. Waddell, Mechanochemistry: opportunities for new and cleaner synthesis, *Chem. Soc. Rev.* 41 (2012) 413–447.
- [28] C. Jobbág, T. Tunyogi, G. Pálinskás, Á. Déák, A versatile solvent-free mechanochemical route to the synthesis of heterometallic dicyanoaurate-based coordination polymers, *Inorg. Chem.* 50 (2011) 7301–7308.
- [29] Y. Yang, S. Zhang, S. Wang, K. Zhang, H. Wang, J. Huang, S. Deng, B. Wang, Y. Wang, G. Yu, Ball milling synthesized MnO_x as highly active catalyst for gaseous POPs removal: significance of mechanochemically induced oxygen vacancies, *Environ. Sci. Technol.* 49 (2015) 4473–4480.
- [30] A.P. Amruite, Z. Łódziana, H. Schreyer, C. Weidenthaler, F. Schüth, High-surface-area corundum by mechanochemically induced phase transformation of boehmite, *Science* 366 (2019) 485.
- [31] G. Cagnetta, J. Huang, M. Lu, B. Wang, Y. Wang, S. Deng, G. Yu, Defect engineered oxides for enhanced mechanochemical destruction of halogenated organic pollutants, *Chemosphere* 184 (2017) 879–883.
- [32] H. Lv, N. Wang, L. Zhu, Y. Zhou, W. Li, H. Tang, Alumina-mediated mechanochemical method for simultaneously degrading perfluorooctanoic acid and synthesizing a polyfluoroalkene, *Green. Chem.* 20 (2018) 2526–2533.
- [33] N. Wang, H. Lv, Y. Zhou, L. Zhu, Y. Hu, T. Majima, H. Tang, Complete defluorination and mineralization of perfluorooctanoic acid by a mechanochemical method using alumina and persulfate, *Environ. Sci. Technol.* 53 (2019) 8302–8313.
- [34] Z. Wan, Q. Mao, Q. Chen, Proton-dependent photocatalytic dehalogenation activities caused by oxygen vacancies in In₂O₃, *Chem. Eng. J.* 403 (2021), 126389.
- [35] G. Kresse, J. Furthmüller, Efficiency of ab-initio total energy calculations for metals and semiconductors using a plane-wave basis set, *Comput. Mater. Sci.* 6 (1996) 15–50.
- [36] Furthmüller Kresse, Efficient iterative schemes for ab initio total-energy calculations using a plane-wave basis set, *Phys. Rev. B Condens. Matter* 54 (16) (1996) 11169–11186.
- [37] J. Li, J. Wang, G. Zhang, Y. Li, K. Wang, Enhanced molecular oxygen activation of Ni²⁺-doped BiO_{2-x} nanosheets under UV, visible and near-infrared irradiation: Mechanism and DFT study, *Appl. Catal. B* (2018).
- [38] J.P. Perdew, K. Burke, M. Ernzerhof, Generalized gradient approximation made simple, *Phys. Rev. Lett.* 77 (1996) 3865–3868.
- [39] Blöchl, Projector augmented-wave method, *Phys. Rev. B Condens. Matter* 50 (1994) 17953–17979.
- [40] J. Ren, L. Jiang, Y. Li, G. Zhang, Cobalt doped bismuth oxy sulfide with abundant oxygen vacancies towards tetracycline degradation through peroxyomonosulfate activation, *Sep. Purif. Technol.* 275 (2021), 119100.
- [41] T. Guo, L. Jiang, K. Wang, Y. Li, H. Huang, X. Wu, G. Zhang, Efficient persulfate activation by hematite nanocrystals for degradation of organic pollutants under visible light irradiation: facet-dependent catalytic performance and degradation mechanism, *Appl. Catal. B* 286 (2021), 119883.
- [42] S. Grimme, J. Antony, S. Ehrlich, H. Krieg, A consistent and accurate ab initio parametrization of density functional dispersion correction (DFT-D) for the 94 elements H-Pu, *J. Chem. Phys.* 132 (15) (2010), 154104.
- [43] F. Kong, H. Zhang, H. Chai, B. Liu, Y. Cao, Insight into the crystal structures and surface property of manganese oxide on CO catalytic oxidation performance, *Inorg. Chem.* 60 (2021) 5812–5820.
- [44] Y. Luo, W. Tan, S.L. Suib, G. Qiu, F. Liu, Dissolution and phase transformation processes of hausmannite in acidic aqueous systems under anoxic conditions, *Chem. Geol.* 487 (2018) 54–62.
- [45] W. Yang, Z. Su, Z. Xu, W. Yang, Y. Peng, J. Li, Comparative study of α -, β -, γ - and δ -MnO₂ on toluene oxidation: oxygen vacancies and reaction intermediates, *Appl. Catal. B* 260 (2020), 118150.
- [46] S. Dang, Y. Wen, T. Qin, J. Hao, H. Li, J. Huang, D. Yan, G. Cao, S. Peng, Nanostructured manganese dioxide with adjustable Mn³⁺/Mn⁴⁺ ratio for flexible high-energy quasi-solid supercapacitors, *Chem. Eng. J.* 396 (2020), 125342.
- [47] Z.-G. Zhou, H.-M. Du, Z. Dai, Y. Mu, L.-L. Tong, Q.-J. Xing, S.-S. Liu, Z. Ao, J.-P. Zou, Degradation of organic pollutants by peroxyomonosulfate activated by MnO₂ with different crystalline structures: catalytic performances and mechanisms, *Chem. Eng. J.* 374 (2019) 170–180.
- [48] G. Cagnetta, Q. Zhang, J. Huang, M. Lu, B. Wang, Y. Wang, S. Deng, G. Yu, Mechanochemical destruction of perfluorinated pollutants and mechanosynthesis of lanthanum oxyfluoride: a waste-to-materials process, *Chem. Eng. J.* 316 (2017) 1078–1090.
- [49] L. Cheng, J. Wang, C. Zhang, B. Jin, Y. Men, Boosting acetone oxidation efficiency over MnO₂ nanorods by tailoring crystal phases, *New J. Chem.* (2019).
- [50] X. Li, J. Ma, L. Yang, G. He, C. Zhang, R. Zhang, H. He, Oxygen vacancies induced by transition metal doping in γ -MnO₂ for highly efficient ozone decomposition, *Environ. Sci. Technol.* 52 (21) (2018) 12685–12696.
- [51] S. Rong, P. Zhang, F. Liu, Y. Yang, Engineering crystal facet of α -MnO₂ nanowire for highly efficient catalytic oxidation of carcinogenic airborne formaldehyde, *ACS Catal.* 8 (2018) 3435–3446.
- [52] M. Huguet, M. Debordre, S. Papot, H. Gallard, Oxidative decarboxylation of diclofenac by manganese oxide bed filter, *Water Res.* 47 (2013) 5400–5408.
- [53] H. Zhang, W.R. Chen, C.H. Huang, Kinetic modeling of oxidation of antibacterial agents by manganese oxide, *Environ. Sci. Technol.* 42 (2008) 5548–5554.
- [54] Y. Wang, S. Indrawirawan, X. Duan, H. Sun, H. Ang, M. Tadé, S. Wang, New insights into heterogeneous generation and evolution processes of sulfate radicals for phenol degradation over one-dimensional α -MnO₂ nanostructures, *Chem. Eng. J.* 266 (2015) 12–20.
- [55] Y. Wang, H. Sun, H.M. Ang, M.O. Tadé, S. Wang, Facile synthesis of hierarchically structured magnetic MnO₂/ZnFe₂O₄ hybrid materials and their performance in heterogeneous activation of peroxyomonosulfate, *ACS Appl. Mater. Interfaces* 6 (2014) 19914–19923.
- [56] A.H. Mady, M.L. Baynosa, D. Tuma, J.-J. Shim, Heterogeneous activation of peroxyomonosulfate by a novel magnetic 3D γ -MnO₂/ZnFe₂O₄/rGO nanohybrid as a robust catalyst for phenol degradation, *Appl. Catal. B* 244 (2019) 946–956.
- [57] E. Saputra, S. Muhammad, H. Sun, A. Patel, P. Shukla, Z. Zhu, S. Wang, α -MnO₂ activation of peroxyomonosulfate for catalytic phenol degradation in aqueous solutions, *Catal. Commun.* 26 (2012) 144–148.
- [58] J. Huang, Y. Dai, K. Singewald, C.-C. Liu, S. Saxena, H. Zhang, Effects of MnO₂ of different structures on activation of peroxyomonosulfate for bisphenol A degradation under acidic conditions, *Chem. Eng. J.* 370 (2019) 906–915.
- [59] Z. Wang, H. Jia, Z. Liu, Z. Peng, Y. Dai, C. Zhang, X. Guo, T. Wang, L. Zhu, Greatly enhanced oxidative activity of δ -MnO₂ to degrade organic pollutants driven by dominantly exposed {−111} facets, *J. Hazard. Mater.* 413 (2021), 125285.
- [60] X. Dong, X. Duan, Z. Sun, X. Zhang, C. Li, S. Yang, B. Ren, S. Zheng, D.D. Dionysiou, Natural illite-based ultrafine cobalt oxide with abundant oxygen-vacancies for highly efficient fenton-like catalysis, *Appl. Catal. B* 261 (2020), 118214.
- [61] T. Tang, G. Lu, R. Wang, Z. Qiu, K. Huang, W. Lian, X. Tao, Z. Dang, H. Yin, Rate constants for the reaction of hydroxyl and sulfate radicals with organophosphorus esters (OPEs) determined by competition method, *Ecotoxicol. Environ. Saf.* 170 (2019) 300–305.
- [62] M. Zhu, J. Miao, D. Guan, Y. Zhong, R. Ran, S. Wang, W. Zhou, Z. Shao, Efficient wastewater remediation enabled by self-assembled perovskite oxide heterostructures with multiple reaction pathways, *ACS Sustain. Chem. Eng.* 8 (2020) 6033–6042.
- [63] J. Miao, J. Li, J. Dai, D. Guan, C. Zhou, W. Zhou, X. Duan, S. Wang, Z. Shao, Postsynthesis oxygen nonstoichiometric regulation: a new strategy for performance enhancement of perovskites in advanced oxidation, *Ind. Eng. Chem. Res.* 59 (2020) 99–109.
- [64] S. Khan, K.R. Yang, M.Z. Ertem, V.S. Batista, G.W. Brudvig, Mechanism of manganese-catalyzed oxygen evolution from experimental and theoretical analyses of ¹⁸O kinetic isotope effects, *ACS Catal.* 5 (2015) 7104–7113.
- [65] E.H. Appelman, L.J. Basile, H. Kim, J.R. Ferraro, Molecular vibrational spectra of potassium peroxyomonosulfate, KHSO₅ and KHSO₅·H₂O, and of the aqueous peroxyomonosulfate ion, *Spectrochim. Acta A Mol. Biomol. Spectrosc.* 41 (1985) 1295–1300.
- [66] B. Dey, Y.S. Jain, A.L. Verma, Infrared and raman spectroscopic studies of KHSO₄ crystals, *J. Raman Spectrosc.* 13 (1982) 209–212.
- [67] D. Swain, V.S. Bhadram, G.K. Pradhan, S.V. Bhat, C. Narayana, C.N.R. Rao, Superionic phase transition in KHSO₄: a temperature-dependent raman investigation, *J. Phys. Chem. A* 114 (37) (2010) 10040–10044.

- [68] P. Vargas Jentzsch, B. Kampe, V. Ciobot, P. Rösch, J. Popp, Inorganic salts in atmospheric particulate matter: Raman spectroscopy as an analytical tool, *Spectrochim. Acta A Mol. Biomol. Spectrosc.* 115 (2013) 697–708.
- [69] L. Yu, G. Zhang, C. Liu, H. Lan, H. Liu, J. Qu, Interface stabilization of undercoordinated iron centers on manganese oxides for nature-inspired peroxide activation, *ACS Catal.* 8 (2018) 1090–1096.
- [70] P. Zhang, H. Lu, Y. Zhou, L. Zhang, Z. Wu, S. Yang, H. Shi, Q. Zhu, Y. Chen, S. Dai, Mesoporous MnCeO_x solid solutions for low temperature and selective oxidation of hydrocarbons, *Nat. Commun.* 6 (2015) 8446.